JGR Atmospheres

RESEARCH ARTICLE
10.1029/2020JD034527

Key Points:

- The first ground-based observation of concentric gravity waves over Brazil is presented
- Spatial and temporal distribution of lightning activities were related to cloud top brightness temperature to locate overshooting plumes
- Periodicities in the lightning flash rate were related to the observed concentric gravity wave periods

Supporting Information:

Supporting Information may be found in the online version of this article.

Correspondence to:
P. K. Nyassor,
prosper.nyassor@inpe.br

Citation:
Nyassor, P. K., Wrasse, C. M., Gobbi, D., Paulino, I., Vadas, S. L., Naccarato, K. P., et al. (2021). Case studies on concentric gravity waves source using lightning flash rate, brightness temperature and backward ray tracing at São Martinho da Serra (29.44°S, 53.82°W). *Journal of Geophysical Research: Atmospheres*, *126*, e2020JD034527. https://doi.org/10.1029/2020JD034527

Received 12 JAN 2021
Accepted 25 APR 2021
Corrected 8 JUL 2021

This article was corrected on 08 JUL 2021. See the end of the full text for details. All corrections have been made to the online version.

Author Contributions:
Conceptualization: P. K. Nyassor, C. M. Wrasse, I. Paulino, S. L. Vadas
Formal analysis: P. K. Nyassor
Funding acquisition: C. M. Wrasse
Methodology: P. K. Nyassor, C. M. Wrasse, K. P. Naccarato, J. V. Bageston
Software: P. K. Nyassor, C. M. Wrasse, C. A. O. B. Figueiredo, D. Barros
Supervision: C. M. Wrasse, D. Gobbi, I. Paulino
Validation: P. K. Nyassor, C. M. Wrasse, D. Gobbi, S. L. Vadas, K. P. Naccarato

Case Studies on Concentric Gravity Waves Source Using Lightning Flash Rate, Brightness Temperature and Backward Ray Tracing at São Martinho da Serra (29.44°S, 53.82°W)

P. K. Nyassor[1], C. M. Wrasse[1], D. Gobbi[1], I. Paulino[2], S. L. Vadas[3], K. P. Naccarato[4], H. Takahashi[1], J. V. Bageston[5], C. A. O. B. Figueiredo[1], and D. Barros[1]

[1]Space Weather Division, National Institute for Space Research, São José dos Campos, SP, Brazil, [2]Department of Physics, Federal University of Campina Grande (UFCG), Campina Grande, PB, Brazil, [3]NorthWest Research Associates, Inc., Boulder, CO, USA, [4]Impacts, Adaptation and Vulnerabilities Division, National Institute for Space Research, São José dos Campos, SP, Brazil, [5]Southern Space Coordination, National Institute for Space Research, Santa Maria, RS, Brazil

Abstract We relate the spatial and temporal distribution of lightning flash rates and cloud top brightness temperature (CTBT) to concentric atmospheric gravity wave (CGW) events observed at the Southern Space Observatory (SSO) in São Martinho da Serra (29.44°S, 53.82°W, 488.7 m) in southern Brazil. The selected identified cases from 2017 to 2018 were observed by a hydroxyl (OH) all-sky imager. Backward ray tracing shows that the time of gravity wave excitation agrees with the highest values of lightning flash rates (indicating lightning jump) as well as the coldest brightness temperatures that indicate the time of convective overshoot. Radiosonde measurements show high convective available potential energy (CAPE), associated with a maximum updraft velocity just prior to the wave events. We find that these possible source locations correspond to the positions and times that convective plumes overshot the tropopause (seen in GOES-16 CTBT images). We also show that higher spatial lightning density (i.e., number of lightning flashes at a given longitude and latitude) agree with the overshoot locations from the GOES satellite. We also find that the overshoot times from the GOES-16 satellite agree with the times lightning jumps were observed in the lightning flash rate. Finally, we find that the periodicities in the lightning flash rate agree with the periods of the observed CGWs, which further strengthens the result that the CGWs were excited by the deep convective systems determined from backward ray tracing.

Plain Language Summary A column of rising warm air (convective plume) in a cloud is capable of vertically overshooting the tropopause into the stratosphere by ∼1–3 km, thereby generating concentric atmospheric gravity waves. The updraft of the plume is the driving factor of the charge separation within the cloud, which results in lightning discharge. Since the lightning flash rate is a direct consequence of the updraft and overshooting, the intensity of the updraft modulates the lightning flash rate. If the plume overshoots the tropopause, the rate of the overshooting is related to the lightning flash rate and also to the waves excited from this overshooting. By backward tracing the waves, the position and time the ray path coincides with the tropopause agrees with the position and time of the overshooting plumes and high spatial density of the lightning. From the lightning flash rate, we also find that lightning jumps occurred at the same times as the overshooting. The spatial and temporal distributions of the overshooting plumes, their respective lightning density, and jumps, the position and time of the ray path as well as the concentric ring centers were used to locate the sources of these concentric waves that we investigate in this work.

1. Introduction

Atmospheric gravity waves can be excited by various mechanisms like tropospheric convection, orographic forcing, wind shear, fronts, and adjustment of jets (e.g., Fritts & Alexander, 2003). Among them, deep convection is dominant in tropical and subtropical regions, where convective clouds generate gravity waves

Writing – original draft: P. K. Nyassor
Writing – review & editing: C. M. Wrasse, D. Gobbi, I. Paulino, S. L. Vadas, K. P. Naccarato, H. Takahashi, J. V. Bageston, C. A. O. B. Figueiredo, D. Barros

(GWs) through: (a) pure thermal forcing, (b) "obstacle" or "transient mountain" effect, and (c) "mechanical oscillator" effect (Fritts & Alexander, 2003; Kim et al., 2003). In contrast, orographic gravity waves are limited to specific geographic morphology, such as mountainous regions. Orographic forcing not only generates gravity waves, but can also facilitate convection processes (Browning et al., 2007; Lean et al., 2009; Smith et al., 2015).

Several observational and modeling results in the past decades have greatly improved our knowledge and understanding of the characteristics of gravity wave excited by deep convection (Alexander et al., 1995a; Lane et al., 2003; Song et al., 2003; Vadas, Taylor, et al., 2009). It is widely accepted that an updraft within a rising warm air envelope (also known as a plume) acts like a vertical mechanical oscillator on the stably stratified lower stratosphere if it overshoots the tropopause, thereby exciting gravity waves that then propagate to the middle and upper atmosphere (Holton & Alexander, 1999; Lane, 2015; Lane et al., 2001; Vadas & Liu, 2009; Yue et al., 2009). The maximum updraft velocity derived from the convective available potential energy (CAPE) (Holton, 1992; Holton & Hakim, 2012) can be used as a proxy to determine the strength of the overshooting and consequently the strength of the excited gravity waves.

Previously published works (e.g., Vadas & Liu, 2009; Vadas et al., 2014) typically used the maximum updraft velocity of the convective plumes to model the updrafts in order to obtain information about the excited gravity wave amplitudes. Lane et al. (2001) modeled convective plumes and showed that the horizontal wavelength of generated waves is related to the width of the convective updrafts. They also found that their frequencies are similar to Brunt-Väisälä frequencies; hence the excited waves have periods as low as ∼5 min. In a model study using convective plume modeling and ray tracing, the effects of winds on concentric rings of gravity waves excited by a convective plume on May 11, 2004 were performed (Vadas, Yue, et al., 2009). They observed that the background wind less than 30 m/s allows the propagation of concentric gravity waves (CGWs) into the upper atmosphere, thereby maintaining its concentric structure. However, background winds greater than 30 m/s, cause concentric shapes to appear elliptical, semi-elliptical, semi-circle, or arc-like. They therefore concluded that background winds greater than 30 m/s have a filtering effect on propagating CGWs and a shape distortion effect as well. The results were compared with waves observed in the hydroxyl (OH) emission by all-sky OH imager. They found that the modeled wave parameters compared well with the wave parameters estimated from the OH images.

The observation of CGWs during the past decades presented major opportunities to study the dynamics of their sources in relation to the generated waves. The first CGWs observed by OH airglow was reported by Taylor and Hapgood (1988). Ground-based observations showed that strong convective activity such as thunderstorms, typhoons/cyclones, etc. were the likely sources of the CGWs (e.g., Azeem et al., 2015; Chou et al., 2017; Sentman et al., 2003; Suzuki et al., 2007, 2013; Taylor & Hapgood, 1990; Vadas & Azeem, 2020; Vadas, Yue, et al., 2009; Vadas et al., 2012; J. Xu et al., 2015; Yue et al., 2009). Also, single or multiple layer satellite observations of CGWs (Perwitasari et al., 2016; J. Xu et al., 2015; Yue et al., 2013, 2014, 2019) found that convective activity was the likely source of many CGWs. Others reported severe weather phenomena, for example, lightning, hail and sprites, during the estimated times the waves were excited (Gong et al., 2015; Sentman et al., 2003; Vadas et al., 2012; J. Xu et al., 2015). Concentric gravity waves excited by earthquakes and volcanic eruptions have been observed. Tsugawa et al. (2011) reported earthquake-generated concentric waves in the total electron content (TEC), and Yu et al. (2015) reported the response of the upper atmosphere to the excited waves. Astafyeva (2019) and Miller et al. (2015) also reported CGWs generated by a volcanic eruption using satellite observations in South America. Finally, partial CGWs have also been observed in the mesopause region during the wintertime over the Southern Andes, and were attributed to secondary GWs from mountain wave breaking (Kogure et al., 2020).

Lightning and hail have been used to indicate the magnitude of the updraft activities during the mature stage of thunderstorm (Atlas, 2016; Deierling & Petersen, 2008; Wang et al., 2015). On the other hand, sprites are an after effect of intense lightning in the upper atmosphere above a storm. Investigation of sources of gravity waves conducted by de Medeiros (2001) and Wrasse et al. (2003) found that intense lightning activities occurred around the likely convective sources and further concluded that the sources and lightning were related. Deierling and Petersen (2008), Wang et al. (2015), and Atlas (2016) showed that updraft and total lightning activity are directly related and also the electric charge density of a convective system is directly proportional to the size of the system (Atlas, 2016; Deierling & Petersen, 2008; Wang et al., 2015).

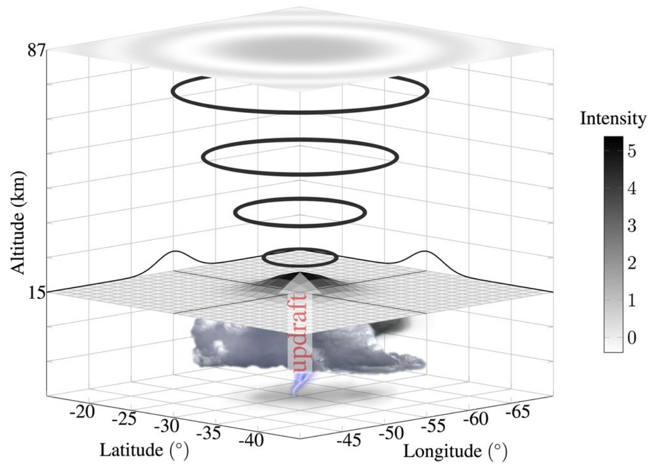

Figure 1. A 3D diagram showing the generation, propagation, and observation of concentric gravity waves. Upward moving air (updraft) is shown as single upward arrow labeled "updraft." The region where the plume updraft overshoots the tropopause and pushes stably stratified stratospheric air upwards is depicted by the bulge shape above the tip of the arrow. Concentric waves are generated after this displaced air is pulled down via gravity. These waves then propagate upward with increasingly larger concentric rings with altitude (the black circles). The concentric patterns are observed in the OH emission layer (87 km) in 2D image as the grey and white concentric rings.

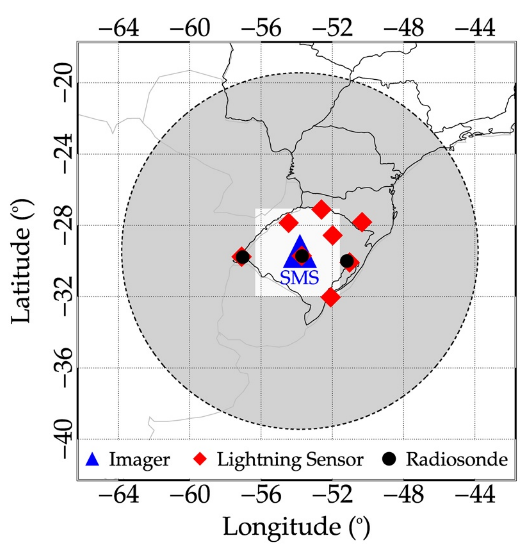

Figure 2. Map showing the locations of the instruments at São Martinho da Serra (29.44°S, 53.82°W). The blue filled triangle, red filled diamonds, and black filled circles show the locations of the imager, BrasilDAT lightning sensors, and radiosondes, respectively. The field of view of the imager is depicted by the white square region within the light gray region, whereas the light gray region within the black dashed-line circle shows the region within which the convective and lightning activities are examined.

The current work is the first ground-based observational study of CGWs in Brazil. We study here three CGW events as case studies. This is also the first study that specifically relates observed wave periods with the periods of the source mechanism using lightning data. Here, the main results of simultaneous and colocated observation of CGWs, GOES-16 cloud top brightness temperature (CTBT) infrared imagery and lightning activities at São Martinho da Serra (29.44°S, 53.82°W) are presented and discussed. The potential propagation path in space and time leading to the likely source positions and times of CGW excitation were determined using backward ray tracing.

2. Morphology of CGWs in a 3D View

As a convective plume impinges on the stably stratified stratosphere, CGWs are excited via diabatic forcing (i.e., latent heating and cooling) and nonlinear forcing (e.g., Lane et al., 2001). A dry air simulation of the excited CGWs can utilize the mechanical oscillator mechanism (Stull, 1976). The generation, propagation, and observation of CGWs in the mesopause region have been modeled using a convective envelope model and ray tracing (Vadas & Fritts, 2009; Vadas, Yue, et al., 2009; Vadas et al., 2012). We illustrate this mechanism in 3D with the inclusion of lightning in Figure 1. This illustration, from the generation of CGWs through their propagation to observation is similar to the 2D illustration by Vadas, Yue, et al. (2009) (their Figure 2).

We include lightning in our study because of published studies (listed above), which show a direct relation between lightning activity and convective updrafts during severe weather such as thunderstorms. In Figure 1, the tropopause is set at 15 km with the stable tropopause layer denoted by the stretched gray mesh. A convective updraft (indicated by the upward arrow labeled "updraft") within the thunderstorm is overshooting the tropopause. Assuming that the updraft is strong enough to push the air in the lower stratosphere upward, concentric GWs are generated which propagate upward. These concentric rings expand outward radially with height from the overshooting point. The region where the plume overshot the tropopause is indicated by the dark-bulge region at the tip of the arrow. The intensity scale is shown by the color bar. This figure is centered at the geographic location where the study is conducted. The dark-bulge region is analogous to the coldest brightness temperature region in a GOES infrared CTBT image. The excited waves that are capable of reaching the mesopause (at 87 km) are observed as white and grey concentric bands in the airglow images.

3. Observation and Methodology

Concentric gravity waves were observed in the OH airglow layer using an all-sky imager installed at the Southern Space Observatory (SSO) (owned by the National Institute for Space Research [INPE]), and coordinated by the Southern Space Coordination (COESU/INPE). The observatory is located in the interior of the municipality of São Martinho da Serra (SMS), at latitude 29.44°S, longitude 53.85°W, and at an altitude of 488.7 m from the sea level, in the central region of Rio Grande do Sul, Brazil. Many instruments are operated at SSO/INPE, from which we highlight two panchromatic imagers and two all-sky imagers. Figure 2 illustrates the geographical location of the observation site. The main instrument used in this study is the all-sky imager and its position is represented by the blue triangle. The positions of the Brazilian lightning detection network (BrasilDAT) and radiosondes are depicted by the red diamonds and black filled circles, respectively. Data from the GOES-16 CTBT and BrasilDAT lightning sensors within the light gray region were examined.

The all-sky imager consisted of a fisheye lens, a telecentric lens system, a single filter for hydroxyl-near infrared (OH-NIR) observations (715–930 nm with notch at 865.5 nm) and an objective lens. The incoming light is recorded by a Charge Coupled Device (CCD) camera (SBIG, STL-1001E model) with an array size of 1,024 × 1,024 pixels and 24.6 × 24.6 mm and 50% of quantum efficiency in the near infrared. The image was not binned but cropped to 512 × 512 pixels producing a final image size of 12 × 12 mm on the CCD chip. Each image has an integration time of 20 s with a sampling rate of 38 s, since the imager does not have a filter wheel (Bageston et al., 2009; Nyassor et al., 2018). Airglow observations at São Martinho da Serra were made when the Sun and Moon elevations are lower than −12° and 10°, respectively, thereby allowing 28 nights of observation per month centered at new moon.

BrasilDAT network is an integrated intracloud (IC) and cloud-to-ground (CG) lightning detection system (total lightning) that combines wide-band sensors and relative dense network deployment of Earth Networks technology. The sensors use a time-of-arrival (TOA) method of detection which enables simpler calibration than direction finding since it is much easier to calibrate timing than bearing, thus reducing potential error in locating lightning events and improving detection efficiency and location accuracy. Exceptional efforts were made to reduce system noise and to broaden the frequency range in order to create an integrated unit capable of detecting both CG and IC discharges with high detection efficiencies. The sensors operate in the 1 Hz to 12 MHz range. CG lightning has been found to radiate at lower frequencies, while IC activity radiates at medium and higher frequencies. Estimates show that BrasilDAT has presently 85%–90% CG detection efficiency, about 50%–60% IC detection efficiency, and about 500 m CG location accuracy.

The GOES-R primary instrument is the Advanced Baseline Imager (ABI), which is an imaging radiometer with 16 different spectral bands, including two visible channels, four near-infrared channels, and 10 infrared channels. These channels have spatial resolution of 0.5–2 km, covering visible and infrared wavelength regions that allow the generation of dozens of critical weather and climate products. The CTBT product is derived from the 11, 12 and 13.3 μm infrared observations and is produced every 15 min for Full Disk, and every 5 min for mesoscale.

In order to obtain the gravity wave parameters: horizontal wavelength (λ_H), period (τ), phase speed (c_H), and azimuth (ϕ) from the airglow images, the sequential image preprocessing and spectral analysis procedure described by Garcia et al. (1997) and Wrasse et al. (2007) was employed. In preprocessing, the original airglow image was aligned to the geographical north, the stars were removed, then unwarped and finally mapped onto the geographical coordinates. Regions of interest (ROI) with visible waves (clear dark and bright bands) were then selected as shown in Figure 3 left panel. Afterwards, a time series of 10 images was constructed with the selected ROI shown in Figure 3 right panel. A two dimensional discrete Fourier transform (2D-DFT) was then applied to the ROI in the selected time series images. The amplitude and the phase obtained from the cross-spectrum of the 2D-DFT were used to estimate the horizontal wavelength, observed period, horizontal phase speed and propagation direction. More information on the spectral analysis can be found in Wrasse et al. (2007), Bageston et al. (2011), and Giongo et al. (2020). Usually only one region of interest is selected for waves with linear wavefronts. However, in the case of concentric wavefronts, the spectral analysis was performed within at least three distinct regions. This was done to determine, if similar waves were propagating through all three of the selected regions (R_1, R_2, R_3) as shown in Figure 3. In that case, the wave parameters were extracted within these three regions for the March 24th, 2018 CGWs event. Note that the wave parameters are only expected to be nearly identical in each region if the background wind is negligible. The winds during this event ranged from 15.00 to 24.45 m/s and peaks at 24.45 m/s in the northeastern part of the image. The mean values of the wave parameters are then obtained from the three regions. The results after the application of the spectral analysis to R_1, R_2, and R_3 are summarized in Table 1.

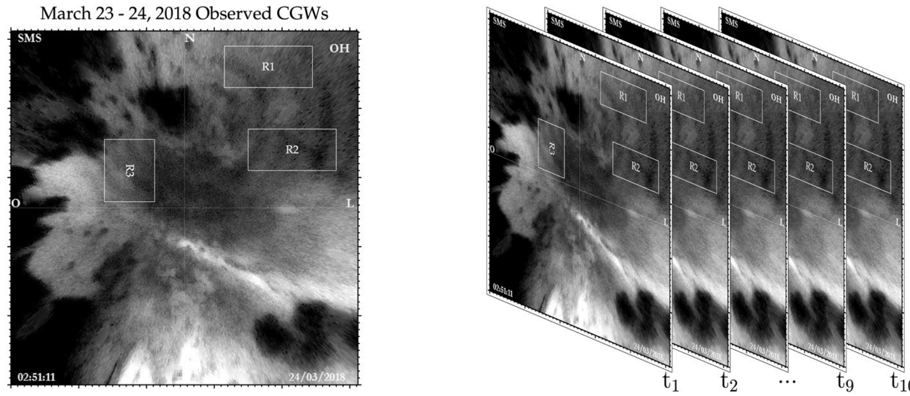

Figure 3. Preprocessed image with selected regions of interest (left panel) used in the calculation of the gravity wave parameters are labeled as R_1, R_2, and R_3. The clouds passing across the field of view of the imager are the dark structures in the image. The bright strand extending from the south-eastern part of the image to the north-western part is the Milky Way. Sequential time series images (right panel) to be used in the spectral analysis.

3.1. Determination of the Center of CGWs

CGWs propagate upward and radially outward from their center; this center corresponds to the possible source of the CGWs when the background wind is zero (or negligible). Therefore, it is important to determine the center since it helps indicate the possible source of the waves and also illuminates the wind effect on wave propagation. Therefore, we determine the centers of the concentric wave structures, then estimate the radius to the first concentric crest/trough of the concentric pattern. To determine the center of CGWs with circular/arc-like wavefronts, we employ the geometric technique based on the concept of intersection between three circles (Pedoe, 1995). In this approach, three circles with similar radius were drawn on the circumference of the circle with unknown center as shown in the left-hand panel of Figure 4. The center of the main circle is then determined as the intersection point for lines 1 and 2. The radius was then estimated by constructing right-angle triangle using lines 1, 2, and 3. Using this procedure, the CGWs event on March 24, 2018 is shown on the right-hand panel of Figure 4. Here, the red-filled circle is the determined center and the orange circle overlays the first crest from the estimated radius.

3.2. Ray Tracing Model

Ray tracing was employed to investigate the CGW source locations. The ray tracing model used in this work follows the approach of Vadas (2007) and Paulino et al. (2012). The approach employs the formalism from Lighthill (1978). However, the group velocities and the dispersion relations are taken from Vadas and Fritts (2005), in order to incorporate kinematic viscosity and thermal diffusivity (Vadas, 2007).

The initial position and altitude of the wave is assumed to be the location (longitude/latitude) of the first visible crest/trough at the altitude of 87 km at the time the wave was observed, and the wave characteristics are used as the input parameters for the model. In determining the next position (longitude, latitude, and altitude) and time, the technique used to solve the six ordinary differential equations was the fourth order Runge-Kutta (Press et al., 2007). An initial step size of 0.2 km was chosen and the subsequent step sizes

Table 1
Parameters of Circular Gravity Waves Observed on March 24, 2018 at São Martinho da Serra

Region (R)	Initial time (hrs)	Final time (hrs)	# of images	Radius (km)	λ_H (km)	ϕ (°)	τ (min)	c_H (m/s)
R_1	02:41	02:53	10	104.6	30.80 ± 1.30	031.0	6.90 ± 0.3	74.40 ± 4.3
R_2	02:41	02:53	10	104.6	31.32 ± 1.05	095.5	7.20 ± 0.5	72.50 ± 2.7
R_3	02:41	02:53	10	104.6	30.56 ± 1.00	198.0	7.06 ± 0.3	70.63 ± 3.1

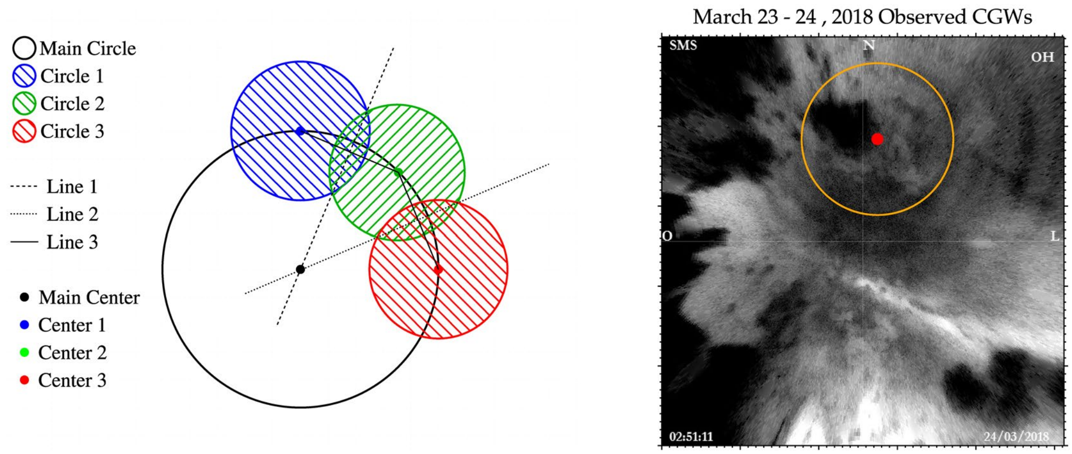

Figure 4. The geometric technique (left panel) used in determining the center and radius of the concentric (circle and arc) gravity waves and the result (right panel) after the application of the technique.

were estimated using the relation $z = c_{g_z} t$ with similar boundary conditions described by Paulino (2012). To perform the iteration for the next step, the following stopping conditions were defined:

1. the group velocity should be less than or equal to 0.9 times the speed of sound ($c_g \leq 0.9C_s$)
2. the real component of the intrinsic frequency must be greater than zero ($\omega_{Ir} > 0$)
3. the momentum flux at all points of the wave trajectory must satisfy the expression:

$$R_m > 10^{-15} R_0, \tag{1}$$

where R_m is the momentum flux at each altitude and R_0 is the momentum flux at the reference altitude. The factor 10^{-15} was arbitrarily chosen

4. the module of the vertical wavelength must be less than viscosity scale $\left(|\lambda_z| < \frac{2\pi}{\frac{d\nu / dz}{\nu}} \right)$

It is important to note that, items (3) and (4) are important when forward ray tracing the waves into the thermosphere. To determine the next time increment of the ray path, the gravity waves must satisfy the above listed conditions. If any of these conditions are violated, the procedure will be interrupted and all calculations automatically saved. Further details on the stopping conditions are discussed in Vadas (2007) and Paulino et al. (2012).

Atmospheric background parameters were obtained from the Modern-Era Retrospective and analysis for Research and Application-version 2 (MERRA-2) data (Gelaro et al., 2017), the Horizontal Wind Model 2014 version (HWM14) (Drob et al., 2015), and the Mass-Spectrometer-Incoherent-Scatter (NRLMSISE-00) empirical atmospheric model (Picone et al., 2002). Due to the altitude range of the MERRA-2 which extended from 0–75 km, we concatenated the MERRA-2 wind data with HWM14, interpolated at each 1 km, in order to attain the altitude range from near the surface of the ground to 100 km. To minimize any discontinuities at the altitude of concatenation, an altitude range of 65–75 km was set for MERRA-2 and HWM14 winds. The difference between the two winds at each kilometer within the set range was estimated, then the altitude with the smallest difference is chosen as the concatenation altitude. The concatenated profile was then smooth at each three points. Since MERRA-2 has a temporal resolution of 3 h, interpolation was performed for each time step. Using the backward ray tracing mode, the wave propagation through the atmosphere was studied and also the wave source location was estimated. In running this ray tracing model, two wind models were considered. In Wind Model 1 (WM_1), the ray tracing model was run with zero wind and in Wind Model 2 (WM_2), the concatenated MERRA-2 and HWM14 wind were included in the model. The individual ray trace results for the three case studies are presented next in the results and discussion section.

Table 2
Concentric Gravity Waves Parameters of the Selected Case Studies at São Martinho da Serra

	Case 1	Case 2	Case 3
Wave Parameters	10/01/2017	03/24/2018	10/18/2018
λ_H (km)	48.20	31.32	44.90
ϕ (°)	48.60	95.50	105.30
c_H (m/s)	60.20	72.50	76.10
τ (min)	13.30	07.20	09.80

4. Results and Discussion

Airglow observations were obtained and examined to identify CGWs from April 22, 2017 to December 31, 2018, resulting in 525 nights of data. However, only 203 nights had clear sky conditions, from which six concentric gravity waves were observed.

Among the six concentric waves, three were eliminated because they satisfied one or more of the following criteria: (a) there were less than three visible concentric wave crest/trough patterns on the image; (b) the horizontal wavelengths were less than 10 km; and (c) no convective system was observed prior to the wave event. CGWs without prior convective activity were excluded, since the main focus of this work is to establish a direct relationship between the convective system (source), and an observed parameter that is directly related to the system (which in this case is lightning). However, note that CGWs which are not associated with deep convection have been observed (Kogure et al., 2020; Vargas et al., 2016). In particular, Kogure et al. (2020) observed secondary GWs with concentric ring structures during the wintertime. They concluded that these CGWs were created by the breaking of mountain waves over the southern Andes. During that event, no convective activity was observed. CGWs considered for this study and their main observed characteristics are presented in Table 2.

4.1. The Observed CGWs Cases

Gravity wave on 10/01/2017 (hereafter Case 1) propagated for about 1.50 h starting 06:44:27 UT, whereas the GWs on 03/24/2018 (hereafter Case 2) and 10/18/2018 (hereafter Case 3) lasted for about 40 minutes. The time interval within which the waves were visible in the all-sky images for Case 2 ranges between 02:29:34 UT and 03:10:06 UT and for Case 3 between 05:36:10 UT and 06:16:48 UT. Figure 5 shows unwarped OH images, where the location of the observatory is shown by the white triangle at the center. The left, middle, and right panels show Cases 1, 2, and 3, respectively. Also, Movie S1, Movie S2, and Movie S3 in the supporting information give the animation of the unwarped OH airglow images for Cases 1, 2, and 3, respectively.

A ray tracing model was used in the reverse mode in order to calculate the gravity wave trajectories back to its source locations in the troposphere. Figure 6 shows the ray tracing results for the CGWs events. For each event, the ray path using no wind is depicted by the red solid line, while the blue solid line is the trajectory of the wave with the model wind. The red and blue filled circles at the end of the ray paths show where

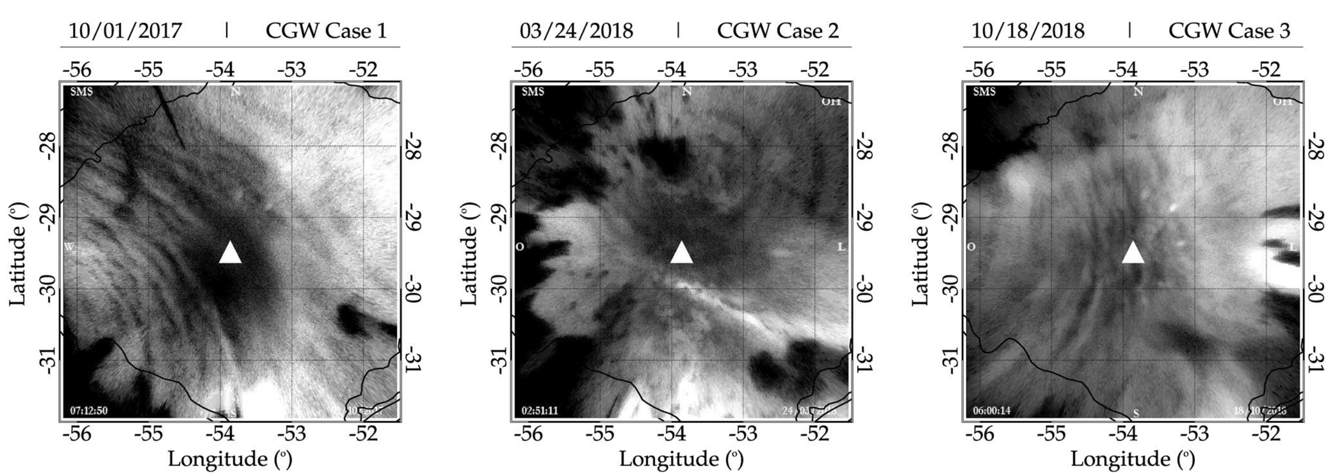

Figure 5. Unwarped hydroxyl (OH) images of the concentric gravity wave events observed in São Martinho da Serra at the Southern Space Observatory (SSO) of National Institute for Space Research (INPE). The white triangle shows the location of the SSO/INPE observatory and the black solid lines extending across the corners are the Rio Grande do Sul state borders.

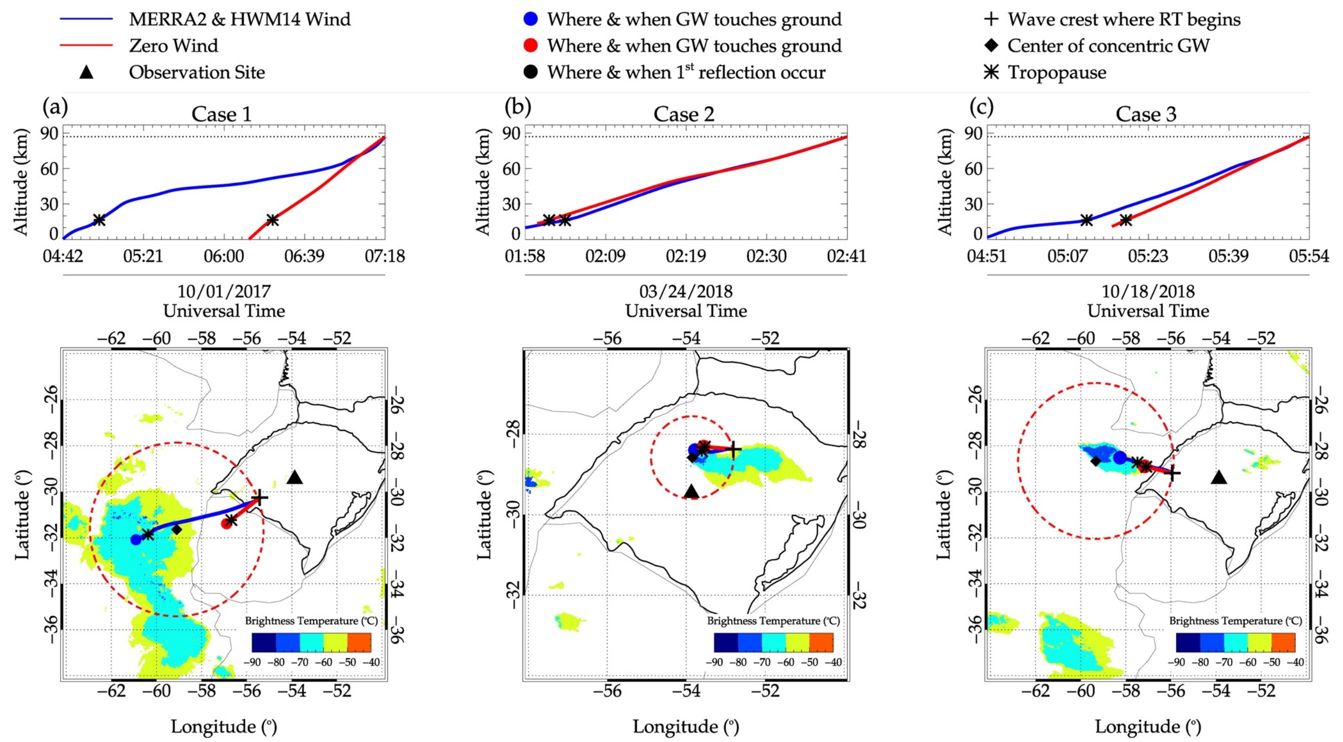

Figure 6. Ray tracing results of the three concentric gravity wave events. Time variation of the gravity wave ray path with altitude is presented in the upper panels, whereas the longitude and latitude variation of the ray paths are shown in the lower panels. (a) is CGW Case 1, (b) is CGW Case 2, and (c) is CGW Case 3.

and when the ray paths stopped. The black asterisks over-plotted on the ray paths of wind models 1 and 2 show the location (longitude/latitude) of the ray when it was closest to the tropopause (see Table 3), thus indicating likely locations/times where/when each GW may have been generated from. The black plus sign shows the point (longitude, latitude, and altitude) where the ray tracing began. The location of the observatory is shown by the black triangle, and the black diamond represents the center of the red dashed circle conforming to the first concentric gravity wave crest on the image. The black dotted lines (in the upper panels) depict the altitude of OH airglow emission layer. Since high frequency concentric gravity waves are generated by overshooting of strong convective updrafts during thunderstorms (Alexander et al., 1995b; Azeem et al., 2015; Holton & Alexander, 1999; Song et al., 2003; Vadas, Taylor, et al., 2009; J. Xu et al., 2015; Yue et al., 2009), the CTBT images corresponding to the position and time when the wave trajectory reached the tropopause were over-plotted together with the ray paths in the lower panels of Figure 6.

From the ray tracing results, two wind models showed when and where the ray path of each gravity waves stop. The ray path of Wind Model 1 and Wind Model 2 for the Case 2 and Case 3 ended below the tropopause except that of Case 1. In Table 3, the locations of the GWs when they were at the altitude of the tropopause are presented. These indicate likely locations where the CGWs may have been created from.

We first consider the ray paths using Wind Model 2. Variation in the ray path is expected since the wave propagation in the atmosphere is mainly determined by the background wind (Vadas, Yue, et al., 2009;

Table 3
The Locations of the concentric gravity waves (CGWs) at the Tropopause Altitude From Reverse Ray Tracing

	Case 1		Case 2		Case 3	
Wind models	Longitude	Latitude	Longitude	Latitude	Longitude	Latitude
1	56.68°W	31.23°S	53.61°W	28.42°S	57.10°W	28.91°S
2	60.37°W	31.86°S	53.61°W	28.42°S	57.48°W	28.73°S

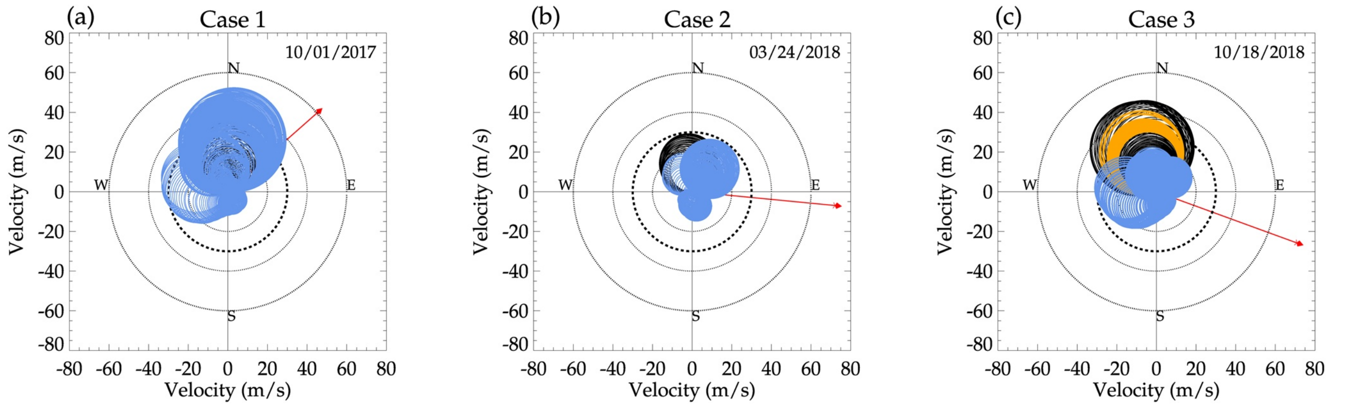

Figure 7. Magnitude and wind direction obtained from the Wind Model 2 used in the ray tracing during the three concentric gravity waves (CGWs) events. The red arrow shows the magnitude and direction of the wave. The light blue regions represent the magnitudes and directions of the wind above the tropopause up to the hydroxyl (OH) emission layer, whereas the black circles depict the wind below the tropopause. The orange circles in (c) indicate the wind from the tropopause to 30 km. The dotted circles show the velocity in intervals of 20 m/s, while the black dashed circles show this quantity in intervals of 30 m/s.

Wrasse et al., 2006, 2007). As established by previous works (e.g., Vadas, Yue, et al., 2009; Vadas et al., 2012; J. Xu et al., 2015; Yue et al., 2009), a weak wind smaller than 30 m/s is a favorable background condition to allow for the propagation of CGWs to the mesopause region without suffering significant wave filtering and the significant distortion of the wave structures. Indeed, a weak background wind was observed during CGWs Cases 2 and 3, although not during Case 1. The magnitude of the zonal wind in Case 1 varied significantly from −12 m/s to 52 m/s. This explains the differences in the ray paths of Wind Models 1 and 2. These results (for the Wind Model 2) are quite consistent with the location of the thunderstorms as indicated by the CTBT images overplotted in Figure 6 (lower panel); thus we conjecture that the CGWs were generated just above the tops of the clouds and propagated up to the mesosphere.

However, the horizontal phase speed of the CGWs are larger than the wind magnitude in all directions. Figure 7 shows a 2D blocking diagram for the CGWs using Wind Model 2. To construct the blocking diagram, following the procedure of Taylor et al. (1993), the intrinsic frequency of the wave was obtained using,

$$\Omega = \omega - k_H U_H = \omega\left(1 - \frac{U_H}{c_H}\right), \tag{2}$$

where ω is the observed frequency of the wave, k_H is the magnitude of the horizontal wave vector, U_H is the wind along the wave propagation direction (ϕ), and c_H is the observed horizontal phase speed of the wave. Expanding the right-hand side of Equation 2 into zonal and meridional wind components (U_x, U_y), we have,

$$\Omega = \omega\left(1 - \frac{U_x \cos\phi + U_y \sin\phi}{c_H}\right). \tag{3}$$

At the critical layer when U_H approaches c_H and Ω approaches zero, Equation 3 then becomes

$$c_H = U_x \cos\phi + U_y \sin\phi \tag{4}$$

Equation 4 represents c_H for every known azimuth of U_x and U_y in a polar plot shown in Figure 7.

The red arrows show the magnitude and direction of the horizontal phase speed of the wave. The blocking diagrams were constructed using the wind profile obtained from the ray tracing paths, which changes in time and height according to the dynamics of the ray path. The wind blocking regions from the ground to the tropopause are represented by the black regions, whereas the light blue regions depict the wind from the tropopause to the mesopause. The dashed circles show the velocity at 30 m/s, whereas the dotted circles show the velocities at 20, 40, and 60 m/s.

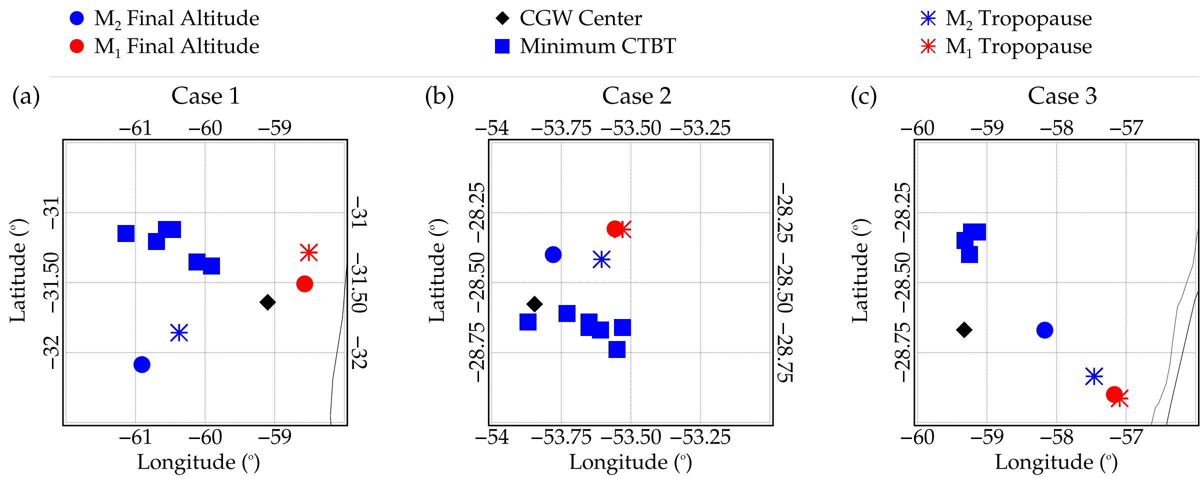

Figure 8. The distribution of the coldest cloud top brightness temperature (CTBT) region, the final ray path and tropopause position. The blue squares show the positions of the coldest CTBT. The red and blue filled circles depict the final positions of the Wind Models 1 and 2 from ray tracing the gravity waves (GWs). The red and blue asterisks show the tropopause positions from Wind Models 1 and 2.

For CGW Case 1, a maximum northward wind speed of ∼50.0 m/s was observed, whereas the phase speed of the wave was 60.0 m/s. However, the blocking diagram shows that the wind speed was less than 30.0 m/s in the northeastern to southwestern direction. It is possible that the propagation direction of the wave was slightly within the forbidden region and as a result suffered some degree of absorption. This could have affected the vertical propagation of the wave, thereby causing a shallower horizontal propagation path seen in the backward ray tracing (see Figure 6a lower panel).

The blocking diagram of Case 3 showed a similar behavior as Case 1 except that the propagation direction of the wave was almost opposite to the forbidden region. The forbidden region has a maximum wind magnitude of ∼45 m/s in the northwestern direction, whereas the phase speed of the wave was 76.1 m/s toward the southeast. The blocking diagrams of these two cases clearly reveal that no significant filtering and structure distortion effect occurred, hence the observation of the concentric waves. However, this has rather favored a longer horizontal propagation as observed in their respective ray tracing results. On the other hand, the blocking diagram of Case 2 showed that the wind magnitude was less than 30 m/s in all directions from the ground to the OH emission layer. As a result, almost a 360° concentric pattern was observed in middle panel of Figure 5 since little/no filtering occurred. Some regions of the concentric pattern were not clear due to the cloud coverage (J. Xu et al., 2015; Yue et al., 2009), which in turn affected the contrast of the image, and other regions were due to dissipation. It is important to note that the two methods used to determine the source (i.e., estimated center and ray tracing) are located at almost the same position as shown in Figure 6b. One indication that confirms weak winds is that the position of the ray path of Wind Model 1 is similar to that of Wind Model 2. The wind characteristics and effect on the CGW Case 2 is in agreement with previous modeled works where almost 360° concentric patterns were seen (Vadas, Yue, et al., 2009; Vadas et al., 2012).

To investigate whether overshooting was the possible excitation mechanism of these CGWs events, the tropopause altitudes were obtained from the nearest (longitude and latitude) radiosonde launch sites. The closest radiosonde launch sites for the Cases 1, 2, and 3 were located at Cordoba (64.21°W, 31.30°S), Santa Maria (53.87°W, 29.48°S), and Uruguaiana (57.03°W, 29.78°S), respectively. For these sites, the respective tropopause altitudes were 17.12, 16.33, and 16.39 km. The respective values of the minimum CTBT are plotted in Figure 8. The tropopause temperatures, the times corresponding to the CGWs events, the locations of the radiosonde launch sites, the tropopause altitudes and the times the ray paths reach the tropopause determined from the radiosonde measurement are summarized in Table 4.

The positions and times when the Wind Model 2 ray paths of the waves reached the tropopause were used to obtain the GOES-16 infrared CTBT image. Furthermore, to know the exact positions of the overshooting tops, the longitudes and latitudes of minimum CTBT that is, the proxy for identifying overshooting tops

Table 4
Summary of the Radiosonde Measurements, Time of Wave Excitation Determined by the Ray Tracing and the Minimum Cloud Top Brightness Temperature (CTBT) (Proxy of the Overshooting Tops)

		Case 1	Case 2	Case 3
Gravity wave event		10/01/2017	03/24/2018	10/18/2018
Latitude	(°S)	31.30	29.48	29.78
Longitude	(°W)	64.21	53.87	57.03
Trop. Alt	(km)	17.12	16.30	16.39
Excitation time	WM_1 (UT)	06:24	02:01	05:19
	WM_2 (UT)	05:00	02:03	05:12
Equation 5	(UT)	04:24	02:01	04:34
Trop. Temp	(°C)	−65.30	−65.32	−77.00
CAPE	(J/kg)	767–877	1,887–2064	2,554–2,779
CTBT Range	(°C)	−74−−70	−76−−71	−85−−86

Abbreviations: CAPE, convective available potential energy; CTBT, cloud top brightness temperature.

(Bluestein et al., 2019) were determined ±30 minutes from the estimated excitation times determined by the Wind Model 2 ray paths. The determined positions are presented in Figure 8. Additionally, the overshooting tops are depicted by blue squares, the estimated centers of the CGWs by black diamonds, the final ray paths positions by blue and red filled circles and the tropopause altitudes by blue and red asterisks. Overshooting tops in relation to GW generation has been widely explored (e.g., Lane, 2015). The point-like nature of the convective overshooting source mechanism on the other hand were found to be the main source of primary GWs with concentric structures in the middle and upper atmosphere (e.g., Yue et al., 2009, 2013, 2014; J. Xu et al., 2015), where overshooting tops were seen in the CTBT image prior to the observation of the CGW events.

The spatial distributions of the coldest CTBT suggests that the overshooting of the tropopause is likely the source of the CGWs. For Wind Models 1 and 2, the Wind Model 2 final ray paths and tropopause positions were found to be in close proximity to the overshooting tops, especially for Cases 1 (Figure 8a) and 2 (Figure 8b) events. The distance between the tropopause positions estimated by the Wind Model 2 ray paths and the closest coldest CTBT are ~73 km and ~25 km for Case 1 and Case 2, respectively. The October 18, 2018 event on the other hand presented a slightly different CTBT distribution in relation to the tropopause position (blue asterisk) which is ~212 km away from the central CTBT region (Figure 8c). This could be due to the fact that the MERRA-2 winds below 70 km and the HWM14 climatology winds above 70 km (monthly averages) will differ from the actual winds. Since the minimum temperature of the CTBT are colder than the tropopause temperatures, it is clear that convective overshoot occurred.

Besides obtaining the excitation time of the gravity waves from the ray tracing model, Equation 5 (Vadas, Yue, et al., 2009; Vadas et al., 2012; Yue et al., 2009) was used to estimate the propagation time from the tropopause to the OH emission altitude assuming zero background wind.

$$\Delta t = \frac{2\pi R^2\left(1 + \Delta z^2 / R^2\right)^{3/2}}{N\Delta z\lambda_H}, \qquad (5)$$

where Δt is the propagation time of the wave from the altitude of excitation to the observation altitude, R is the radius of the CGWs, Δz is the distance between the tropopause altitude and observation altitude, N is the Brunt Väisälä frequency, and λ_H is the horizontal wavelength of the CGW.

Using Equation 5, the excitation times of the CGWs were estimated to be 4 h earlier for CGWs Cases 1 and 3. However, the Case 1 ray tracing results indicated that the wave was excited ~2 h earlier whereas that for Case 3 was excited ~45 min earlier. This discrepancy between the excitation times from ray tracing and from Equation 5 likely occur because Equation 5 is a theoretical estimate of the GW propagation time assuming weak or zero background wind. This assumption, however, is not valid here (see Figure 7), since the wind is greater than 30 m/s.

For Case 2, both the estimated time of wave excitation from Equation 5 and from ray tracing indicate that the CGWs were excited ~40 minutes earlier. This result was expected since the background wind is small and Wind Model 1, Wind Model 2 and the estimated radius all pointed to nearly the same source location. Also the blocking diagram indicated that the wind in all directions during this event was less than 30 m/s (found within the black dashed circle shown in Figure 7b). This result is in good agreement with published results (Yue et al., 2009). These excitation times are also given in Table 4.

4.2. Tropospheric Source

If a convective updraft overshoots the tropopause by 1–3 km, gravity waves are generated (e.g., Lane et al., 2001). In order to know at what altitude this occurred, the vertical extension of the tropopause into the

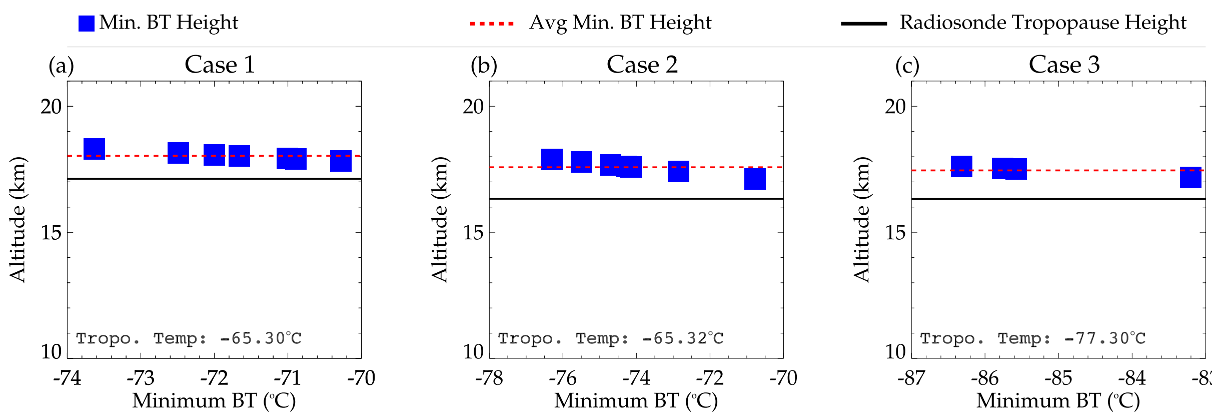

Figure 9. Estimated overshooting tops (minimum cloud top brightness temperature [CTBT]) altitude for concentric gravity wave (CGW) events, (a) Case 1, (b) Case 2, and (c) Case 3. The blue squares represent the estimated overshooting top (OT) altitude for each minimum CTBT, the red dashed line shows the mean OT altitude, and the black solid line depicts the tropopause altitude obtained from the radiosonde measurement.

stratosphere was estimated. Due to lack of observational data to determine the altitude of the overshooting top (OT), we adapted Equation 6 from Griffin et al. (2016). Since the overshooting point is depicted as the coldest region on the GOES CTBT infrared image (Bedka et al., 2010), the tropopause temperature must be hotter than that of overshot CTBT region.

$$OT\ Height = Tropopause\ Height + \frac{OT\ BT - Tropopause\ Temperature}{OT\ Lapse\ Rate}, \tag{6}$$

where the OT lapse rate is assumed to be -7.34 K km^{-1}.

As input parameters in Equation 6, we utilize the tropopause height and temperature obtained from radiosonde measurements in Table 4, as well as the minimum CTBT. On average, the estimated OT altitude revealed that the tropopause was overshot respectively by 1.00 km, 1.20, and 1.30 km for the Cases 1, 2, and 3. Figure 9 shows the tropopause and the average OT altitude. The blue square represents the altitude of the individual minimum CTBT, the red dashed line, the average OT altitude and the black line shows the altitude of the radiosonde tropopause.

Furthermore, the CAPE prior to the time of the overshooting obtained from the radiosonde measurement showed values high enough to produce strong maximum updraft velocities that can result in overshootings. The maximum updraft velocities (w) estimated from the CAPE values presented in Table 4 are obtained by using Equation 7 (Holton, 1992). Maximum updraft velocities between 39–42 m/s, 61–64 m/s, and 71–75 m/s were obtained for Case 1, Case 2, and Case 3, respectively.

$$w \sim \sqrt{2CAPE} \tag{7}$$

Previous literature (e.g., Holton, 1992; Vadas et al., 2012), used the CAPE to estimate the vertical velocity of the updrafts in the convection region. This was then used to estimate the amplitudes of the GWs excited by the updraft (e.g., Vadas & Fritts, 2009). The CAPE can also indicate the size of hail (e.g., Bluestein, 1993) and lightning (Bedka et al., 2010). Stronger updrafts yield larger hail (since these updrafts can hold the hail up longer in the updraft before the hail succumbs to gravity and falls out of the updraft). During the CGWs event at Colorado on the September 8–9, 2005, hail of various sizes were observed with their sizes related to the updraft (Vadas et al., 2012). The authors further showed that the locations of the hail agreed well with the locations of convective overshoot. Bedka et al. (2010), on the other hand, observed strong lightning activity close to the location of the convective overshooting tops.

On this basis, lightning data obtained from the Brazilian lightning detection network (BrasilDAT) sensors were used to investigate lightning activity within the time range of the CTBT image prior to the time of observation of the wave event. Lightning data within a radius of ~1,000 km around the SMS observatory was considered. We chose this range due to the maximum distance in the Wind Model 2 ray path of the wave

10.1029/2020JD034527

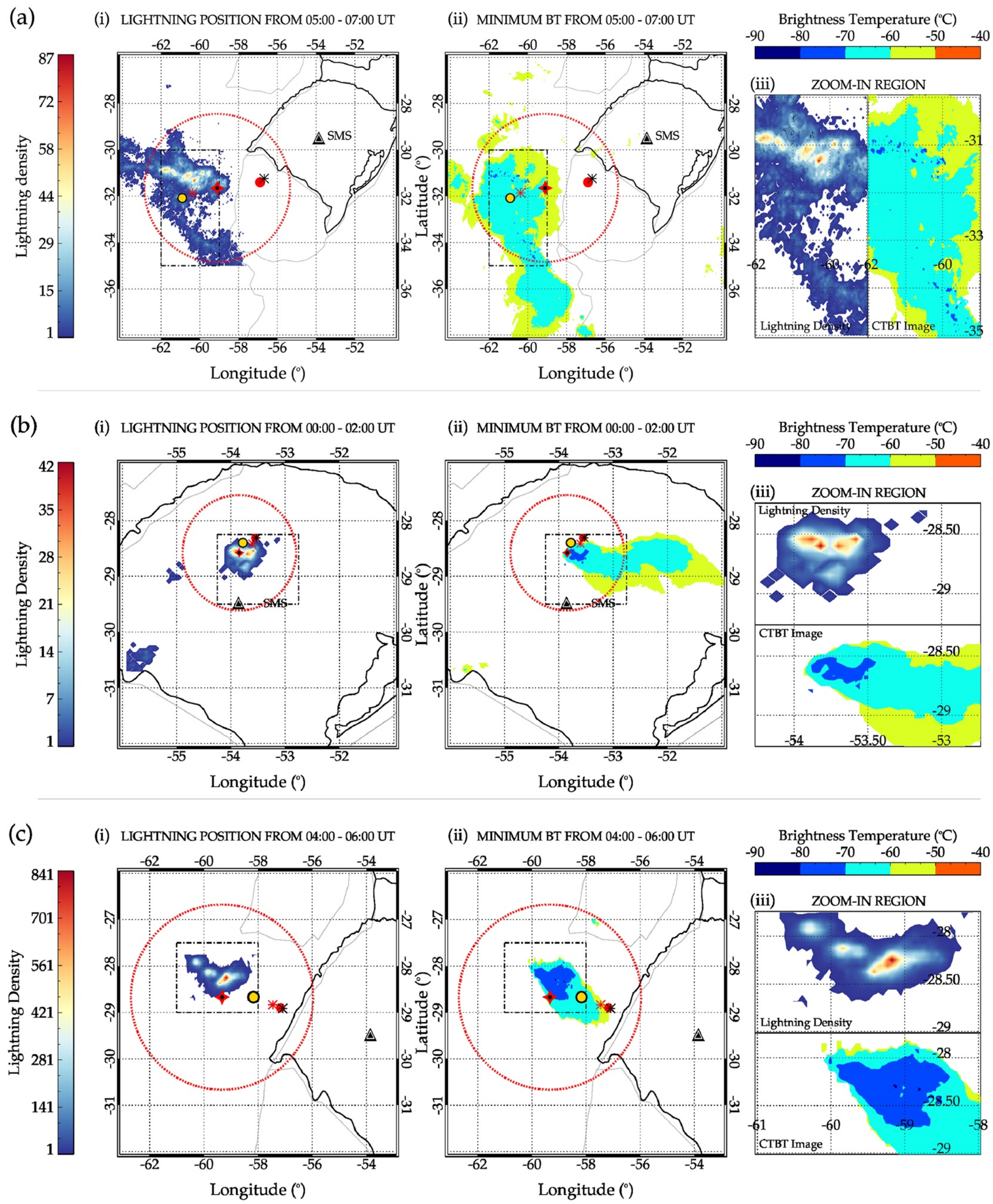

Figure 10. (a) Case 1, (b) Case 2, and (c) Case 3. (i) Comparison between the spatial distribution of the density of lightning flashes and (ii) the overshooting tops (coldest BT region). The gold filled circle with black outline represents the final point of the Wind Model 2 ray path, the red filled circle shows the final point of the Wind Model 1 ray path. The red star with black dot depicts the center of the red dashed circle. The asterisks besides each final ray path positions are the tropopause positions. (iii) Zoom-in of the area depicted by black dashed-dotted lines in (i) and (ii). The red dashed circle is the same as in Figure 6.

from the tropopause. Details on the instrumentation of the BrasilDAT sensors can be found in Naccarato and Pinto (2009) and Naccarato and Pinto (2012). Two main analyses were performed for the lightning data: (a) determination of the spatial distribution by binning in $0.06° \times 0.06°$ grid boxes and (b) estimation of the lightning flash rate. The spatial distribution of the lightning densities and the CTBT of CGW Cases 1, 2, and 3 are presented in Figures 10a–10c, respectively, with the zoomed region denoted by the dashed-dotted lines in the right-hand panels.

In all the three cases of the CGWs, it is clear that the regions with the highest lightning densities in Figure 10 agree with the regions with minimum CTBT (OTs). The results are in accordance with previous works (e.g., Bedka et al., 2010; Jurković et al., 2015) relating OTs (minimum CTBT) to intensive lightning activity. Observational studies by Bedka et al. (2010) showed a considerable amount of occurrence of lightning at close proximity to OTs. Their results further reveal that colder CTBT (>200 K or <−73.15°C) identified by satellite images had greater occurrence of lightning within 10 km radius around the overshooting tops. In central Europe, Jurković et al. (2015) related lightning, OTs, and hails to strong convective storms. They found that there is a significant increase in the lightning strokes at the time of overshooting. For one of the cases studied by Jurković et al. (2015), production of hail was observed and coincidentally the lightning flash rate per minute resulted in a jump from 25 to 92 strokes per minute. Such a drastic change in strokes per minute is an indication of strong updraft (Emersic et al., 2011; Schultz et al., 2009). The lightning activity analysis for these three cases showed similar behavior with the highest lightning activity showing a significant amount of high densities in the region of the OTs for the Case number 3.

Similarly, our result showed that the spatial and temporal distribution of OTs in the BT plot (Figure 10ii) agrees well with the spatial and temporal distribution of the lightning strokes density (Figure 10i). In all plots, the stopping position of the Wind Model 2 ray path, the tropopause position of Wind Model 2 ray path and the determined center are close to the region of high lightning density and the OTs (minimum BT regions). Also, lightning jumps were observed exactly at the times of the coldest region (depicted by blue small structures on the CTBT images with temperature range between −70°C and −80°C) for the Cases 1 and 2, whereas −80°C–−90°C for Case 3.

In order to relate the lightning activity to the OTs and also the periods of the excited waves, the temporal variations in the lightning flash rate were used. To determine the lightning flash rate, the number of lightning flashes per minute was computed by tracking the thunderstorm cell based on the GOES-16 imagery. Also, the window within the lightning was counted, while moving together with the storm. The variation of the lightning flash rate reveals lightning jumps which is an indication of a change in the updraft (Bedka et al., 2010; Jurković et al., 2015). With the time series of the lightning flash rates (shown in Figure 11), the times of occurrence of the lightning jumps were identified and compared to the times when minimum CTBT (or OTs) were seen in the GOES-16 infrared CTBT images.

To follow the time evolution of the OTs using CTBT images, a time series image was constructed including the images that corresponded to the estimated wave excitation time obtained from the ray tracing results. In Figure 11, each image corresponds to the region demarcated by the rectangle on the time-lightning stroke rate plot. The gray shaded regions show the estimated time of the wave excitation (at the tropopause) by the ray tracing model results. Several lightning jumps were observed in the lightning rate for all the events presented. For the CGW Case 1, a significant jump occurred ∼05:00 UT with the second one occurring ∼5 min later. These two jumps occurred within the shaded region that is the estimated time for wave excitation. Beyond that, other jumps were also seen with the highest being within the time frame of 05:45–05:56 UT.

The CGW Case 3, however, indicated that the gravity wave was excited ∼40 min (i.e., around 05:12 UT) before the time of observation (see Figure 6c, upper panel). The lower panel of Figure 6c showed that the estimated excitation location was ∼212 km from the minimum CTBT image corresponding to the time of excitation from Figure 6c (upper panel). Interestingly, the positions of the estimated OTs corresponding to the minimum CTBT from 05:00–05:46 UT showed no significant overshootings. Also, there is no significant jump seen during the estimated time of excitation; it was instead observed at ∼04:30–04:41 UT. The wind speed from the tropopause to ∼30 km ranged between 29 and 38 m/s (the orange regions in Figure 7c) in the northwestern direction. However, our wind model includes climatology winds above 70 km, as mentioned earlier, which only give us a guide of the winds that evening.

For the CGW Case 2, even though the lightning rate values were not as large as that of the Case 1, a lot of jumps were present with a peak at ∼02:07 UT. However, there was no CTBT image at this time, also there was no significant displacement in the position of the convective plume within the set time frame. Cooney et al. (2018) mentioned that the lifetime of an overshooting event spans ∼5–10 min. The estimated wave excitation time, that is, the gray shaded region in Figure 11bii corresponded to the CTBT time frame image of 02:00 UT–02:11 UT, if there was one. Also, Schultz et al. (2009), Bedka et al. (2010), and Jurković

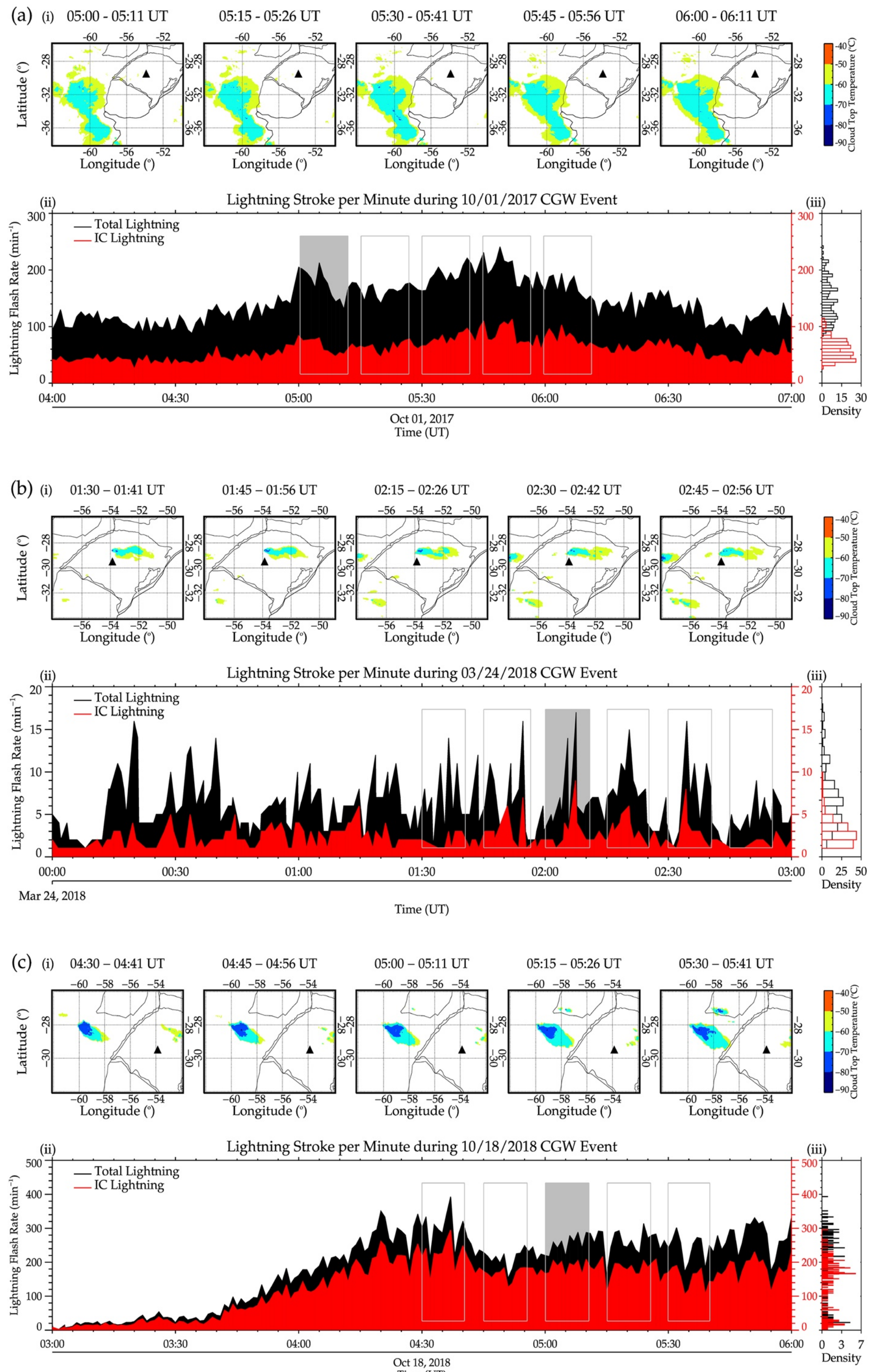

Figure 11. Comparison between image sequence of GOES-16 and the time series of lightning strokes per minutes. The upper (a), middle (b), and lower (c) panels respectively represent the concentric gravity wave (CGW) events for Case 1, Case 2, and Case 3. For each case, (i) represents image sequence of cloud top brightness temperature (CTBT) within the time range of the lightning time series, (ii) shows the time series, and (iii) the densities of the lightning rate of both total and intracloud lightning. The rectangles sequentially represent the CTBT GOES-16 images in (i) and the gray shaded region depicts the time when the wave trajectory reaches the tropopause (the likely excitation time).

et al. (2015) referred to lightning jump as an after effect of the change in the updraft and overshooting event (Bedka et al., 2010; Jurković et al., 2015), therefore, in the absence of CTBT image during this jump yet having 4 min difference in time between the images, it is possible that the image before this jump could have captured the overshooting event, hence using the image before the jump as a reference. Additionally, as mentioned above, the actual winds may have been different from the HWM14 climatology winds above 70 km. Thus, our results are likely within the error bars of the uncertainties in the wind.

As mentioned earlier, the horizontal and vertical wavelengths of the dominant excited GWs are related to the width and depth of a convective plume (Lane et al., 2001; Vadas, Yue, et al., 2009). We can determine the intrinsic period of the dominant characteristic wave generated from this source via Equation 8 (Vadas, Yue, et al., 2009):

$$\tau_c = \tau_b \sqrt{\left(\frac{\mathcal{D}_H}{\mathcal{D}_Z}\right)^2 + 1}, \tag{8}$$

where τ_c is the characteristic period, $\tau_b = 2\pi/N$ is the buoyancy period, $\mathcal{D}_H$ is the width of the plume, and $\mathcal{D}_Z$ is the depth of the plume. Because the depths and widths are similar, the generated GW have periods of 5–15 min, which is close to the Brunt Väisälä frequency, similar to Lane et al. (2001).

In this work, we determined the widths of the plumes (the region of GOES-16 infrared CTBT images with the coldest brightness temperature) and found them to be ∼14–25 km. These values are in reasonable agreement with the typical horizontal extent of convective plume (Vadas et al., 2012). We chose two CTBT images before the image corresponding to the time the ray path of Wind Model 2 reached the tropopause. Estimating the period using Equation 8 and taking the plume's depth to be 10 km (Vadas, Yue, et al., 2009), we obtained periods ranging from 8–14 minutes. These periods are similar to the range of periods of the gravity waves in this study. We now estimate periods in the lightning flash rate oscillations.

Since lightning jumps indicate an updraft (Williams et al., 1999), these jumps may indicate gravity wave generation since this occurs if overshoot occurred (Jurković et al., 2015). One can then say that if all or a majority of the jumps occur when updrafts overshot the tropopause, then the frequency of the jumps can be related to the frequency of the updraft as well as the frequency of the gravity wave generated. Further analysis to determine periodicities were performed on the time series of the lightning flash rate within the set of time intervals presented in Figure 11. Lomb Scargle periodogram (Zechmeister & Kürster, 2009) and wavelet analysis (Torrence & Compo, 1998) were used to determine the periodicities present in the lightning rate.

Before the application of the Lomb Scargle periodogram and wavelet analysis, a residual, that is, the difference between the lightning flash rate and its fit, was estimated. Due to the frequency range of the wave, least squares fitting for frequencies above 30 min were constructed and subtracted from the lightning jump time series. This was done in order to eliminate periods longer than 30 min from the lightning flash rate. Beside considering the time the wave trajectory reached the tropopause as indicated by the ray tracing result, we also took into account the time the lightning jumps occurred since; (a) lightning jump is the best early indicator of a strengthening updraft within a thunderstorm (Carey et al., 2019; Schultz et al., 2009) and (b) the time of the jump positively correlates with the time of overshooting (Jurković et al., 2015). The results of the Lomb Scargle periodogram and wavelet analysis of the lightning flash rate are shown in Figure 12.

In Panel (i) of Figure 12, the time series of the total lightning and its residual are presented with the identified jumps labeled LJ. The occurrence time of the identified jumps and the time of BT image corresponding to those times are shown in Table 5. The times of the lightning jumps are in good accordance with the time the minimum CTBT images were captured. The OT (minimum CTBT) positions also coincide with the region of spatial distribution with highest lightning density as shown in Figure 10. This is expected since lightning activities (lightning jumps) are directly related to updraft and overshooting (Jurković et al., 2015). Several works (e.g., Lane et al., 2001; Vadas, Yue, et al., 2009) through modeling showed the direct relationship between the frequency of the source and the observed gravity wave. Since lightning flash rate variations give information about the temporal variation of updraft (Deierling & Petersen, 2008) and overshoot (Bedka et al., 2010) as demonstrated in Figure 12, the lightning rate frequency (period) for the first time are related to the frequency (period) of the gravity waves generated using observational data.

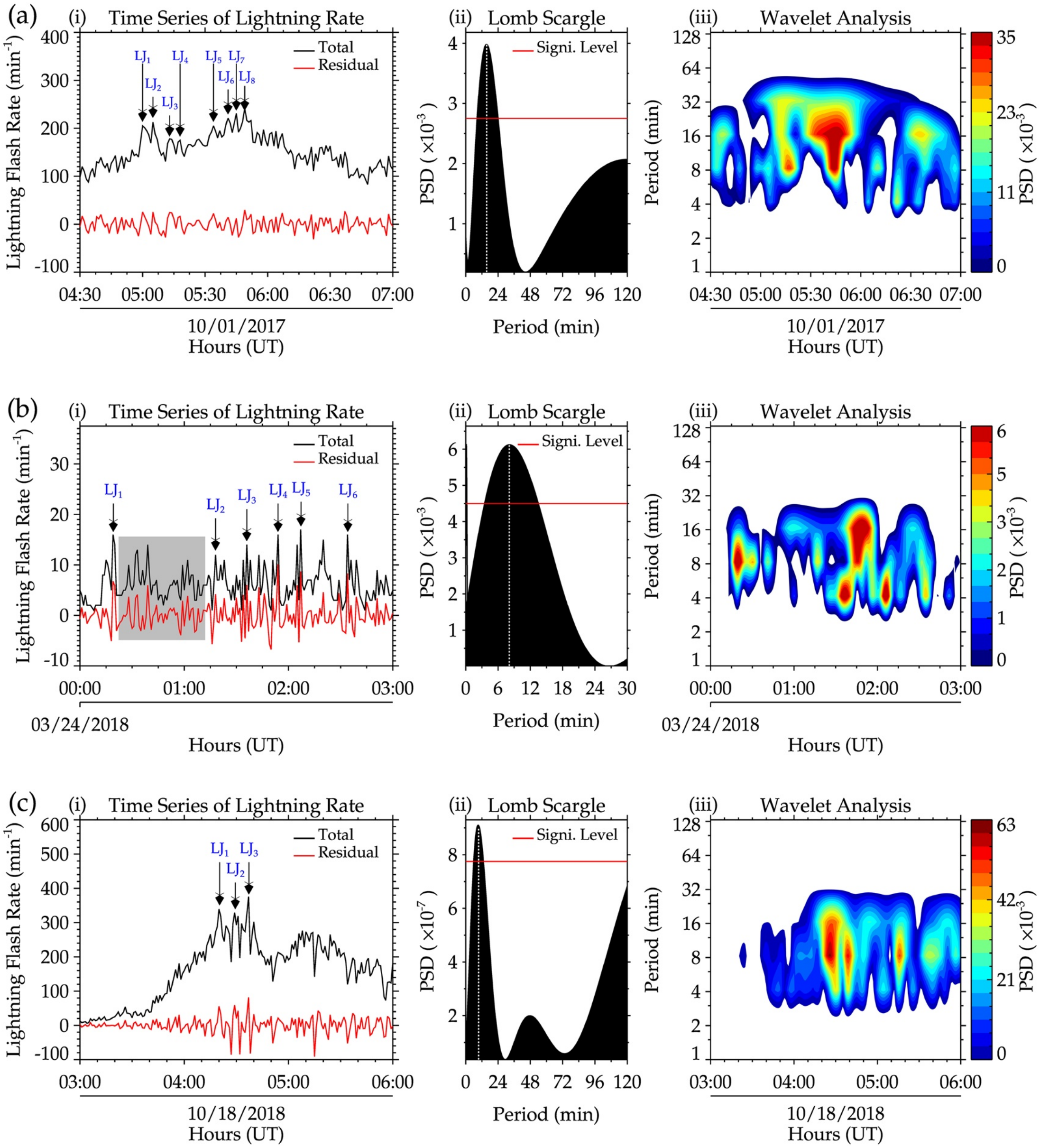

Figure 12. Periodicities in the lightning flash rate. The top (a), middle (b) and bottom (c) represent the concentric gravity wave (CGW) events of Case 1, Case 2, and Case 3, respectively. Panel (i) represent the time-lightning rate plot, whereas in (ii) the Lomb Scargle Periodogram is presented and (iii) showing the wavelet analysis result.

Lomb Scargle periodogram (Figure 12ii for all panels) was applied to both total lightning flash rate and the residual with both showing similar periodicities. Peak periods obtained by the Lomb Scargle periodogram and the wavelet analysis are similar to the periods of the observed waves. The comparison of the results are summarized in Table 6; we note that the period of the gravity wave and those obtained from the lightning flash rate using Lomb Scargle periodogram and wavelet analysis are similar.

5. Summary and Conclusion

The current work presents gravity waves with concentric wave patterns observed in the OH emission layer using an all-sky imager located at São Martinho da Serra (SMS-Brazil). Three cases of CGWs were analyzed, with two cases being arc-like and one case with nearly perfect concentric rings. Backward ray tracing results

Table 5
Summary of cloud top brightness temperature (CTBT) Image in Relation to Lightning Jumps, Their Respective Time of Occurrence and Change in Rate for all the concentric gravity waves (CGWs) Events

	Case 1 (10/01/2017)			Case 2 (03/24/2018)			Case 3 (10/18/2018)		
BT image frame	Jump label	Time (UT)	Rate (min^{-1})	Jump label	Time (UT)	Rate (min^{-1})	Jump label	Time (UT)	Rate (min^{-1})
Frame 1	LJ_1	4:59–5:00	140–205	LJ_3	1:35–1:36	3–14	LJ_1	4:20-4:21	288–339
	LJ_2	5:04–5:05	169–213						
Frame 2	LJ_3	5:11–5:12	131–168	LJ_4	1:53–1:54	8–16	LJ_2	4:27-4:28	185–297
	LJ_4	5:16-–5:17	146–171						
Frame 3	LJ_5	5:31–5:32	164–184	LJ_5	2:06–2:07	3–17	LJ_3	4:35-4:36	274–376
	LJ_6	5:40–5:41	186–221						
Frame 4	LJ_7	5:44–5:45	191–231	LJ_6	2:33–2:34	3–16			
	LJ_8	5:49–5:50	200–241						

showed in all three cases, convective systems were present approximately an hour or more prior to the observation of the CGWs in the OH emission layer. Horizontal wind from MERRA-2 revealed a weak wind profile below 30 km for CGW Case 1. This weak wind effect on the CGWs propagation has been reflected in the final results of the determined source for the two ray tracing wind models (Wind Model 1/Wind Model 2) used. Also, Cases 1 and 3 presented different propagation behavior due to the wind. The spatial and temporal distribution of the convective overshoot (indicated by coldest BT) correlate well with the position and time needed for the wave to reverse ray trace to the tropopause. Also within the time of wave excitation and observation in the mesosphere, spatial distribution of the lightning density showed positive agreement with that of the coldest BT region.

Detailed studies conducted on the source of each case resulted in the following results. For the case on October 1, 2017, the backward ray tracing result showed the position and time where and when the wave was excited. The identified overshooting position by infrared CTBT GOES-16 image coincide with the ray trace position within 0.6° longitude and latitude. The estimated center using the approach described in Section 3.1, deviated from the tropopause position estimated by the ray tracing by 0.2° in latitude and 1.25° in longitude. This deviation between the estimated center and the position of the tropopause (source position determined by ray tracing) was attributed to the MERRA-2 and HWM14 wind profile between the tropopause to the OH emission altitude.

The March 24, 2018 CGWs event ray tracing result indicated that the tropopause position of both Wind Model 1 and Wind Model 2 agreed positively with the determined center and the overshooting tops. These different approaches pointing to one source region affirms that the wind speed was small in relation to the horizontal phase speed of the wave.

The October 18, 2018, on the other hand, had the tropopause position determined by the ray tracing about 212 km away from the closest overshooting tops. Surprisingly, the time of excitation, when the ray path reached the tropopause corresponded to the time when the overshooting of the tropopause occurred. Even

Table 6
Comparison Between the Periods of the concentric gravity waves (CGWs) and Oscillations Obtained From the Lightning Flash Rate Data

			Case 1	Case 2	Case 3
Gravity wave event			10/01/2017	03/24/2018	10/18/2018
Period (min)	Gravity Wave		13.30	07.20	09.80
	Lightning	Lomb Scargle	15.60	08.10	09.60
	Rate	Wavelet	16.40	08.20	08.35

though the backward ray tracing result location of the source is quite far from the probable source, further investigations based on the source characteristics compared to the wave characteristics revealed that the nearby convective system is possibly the source.

Lightning density spatial distribution ±1 hour from the time of wave excitation with the time of OH observation agrees well with the spatial distribution of the coldest BT region within the same time range. From the lightning data, lightning flash rate per minute was used to investigate the variations in the updraft velocity and the occurrence of overshooting based on the linear correlation between lightning flash rate, updraft, and convective overshooting (Bedka et al., 2010; Deierling & Petersen, 2008; Jurković et al., 2015). Since the lightning flash rate reflects strong updrafts, we hypothesize that the frequency (cycle of updraft duration) at which the updraft overshot the tropopause (which will reflect in the lightning flash rate) can be used to obtain the frequency of the waves generated. Indeed we found this to be the case for all the CGWs events discussed above where positive correlations were found between the frequencies of the waves and the lightning flash rate as well as the periods estimated using Equation 8 (Vadas, Yue, et al., 2009).

It can hereby be concluded that lightning flash rate perturbations can most likely be used to estimate the frequency spectrum of excited gravity waves by convective overshoot. It is important to note that this approach can only work for gravity waves excited by convective overshooting of the tropopause. Concentric gravity waves are chosen for this investigation because they are directly linked to updraft, overshoot, and lightning flash rate. J. Xu et al. (2015) reported high CAPE values and high lightning activity (depending on the size of the convective system) during their CGWs observation over China, whereas other researchers used satellite observations for CGWs studies; for example Yue et al. (2014) and S. Xu et al. (2019) observed lightning activity near or some degrees around the centers of the CGWs events reported. Sentman et al. (2003) simultaneously observed lightning strike associated with thunderstorm that generated CGWs over Nebraska. It is, therefore, possible to use lightning data obtained from sensors located near strong thunderstorms to estimate possible frequency/period of waves to be generated and the spectrum of waves to be expected in the upper atmosphere.

Data Availability Statement

The Airglow images from São Martinho da Serra can be accessed online in the portal of the "Estudo e Monitoramento Brasileiro do Clima Espacial" (EMBRACE/INPE) at http://www.inpe.br/climaespacial/portal/en. The cloud top brightness temperature maps were provided at http://satelite.cptec.inpe.br/acervo/goes16.formulario.logic. The radiosonde data were obtained from the University of Wyoming through the link http://weather.uwyo.edu/upperair/sounding.html.

Acknowledgments

This work has been supported by Coordenação de Aperfeiçoamento de Pessoal de Nível Superior (CAPES) and Conselho Nacional de Desenvolvimento Científico e Tecnológico (CNPq). C. M. Wrasse, I. Paulino, H. Takahashi, and D. Barros thank CNPq for the financial support under the contract numbers 314972/2020-0, 306063/2020-4, 310927/2020-0 and 300974/2020-5. S.L. Vadas was supported by NSF Grant AGS-1552315. C.A.O.B. Figueiredo thanks Fundação de Amparo à Pesquisa do Estado de São Paulo (FAPESP) under the process number 2018/09066-8. The cloud top brightness temperature maps were provided by the Center for Weather Forecasting and Climate Studies (CPTEC/INPE). The lightning data were provided by the Brazilian lightning detection network (BrasilDAT) from the Earth Sciences Department (DIIAV/CGCT/INPE) supported by EarthNetworks. The radiosonde data were provided by the University of Wyoming.

References

Alexander, M. J., Holton, J. R., & Durran, D. R. (1995a). The gravity wave response above deep convection in a squall line simulation. *Journal of the Atmospheric Sciences*, *52*, 2212–2226. https://doi.org/10.1175/1520-046910.1175/1520-0469(1995)052<2212:tgwrad>2.0.co;2

Alexander, M. J., Holton, J. R., & Durran, D. R. (1995b). The gravity wave response above deep convection in a squall line simulation. *Journal of the Atmospheric Sciences*, *52*, 2212–2226. https://doi.org/10.1175/1520-0469(1995)052⟨2212:TGWRAD⟩2.0.CO;210.1175/1520-0469(1995)052<2212:tgwrad>2.0.co;2

Astafyeva, E. (2019). Ionospheric detection of natural hazards. *Reviews of Geophysics*, *57*(4), 1265–1288. https://doi.org/10.1029/2019RG000668

Atlas, D. (2016). *Severe local storms* (p. 247). Springer.

Azeem, I., Yue, J., Hoffmann, L., Miller, S. D., Straka, W. C., & Crowley, G. (2015). Multisensor profiling of a concentric gravity wave event propagating from the troposphere to the ionosphere. *Geophysical Research Letters*, *42*, 7874–7880. https://doi.org/10.1002/2015GL065903

Bageston, J., Wrasse, C. M., Batista, P., Hibbins, R., Fritts, D., Gobbi, D., et al. (2011). Observation of a mesospheric front in a thermal-doppler duct over King George Island, Antarctica. *Atmospheric Chemistry and Physics*, *11*, 12137–12147. https://doi.org/10.5194/acp-11-12137-2011

Bageston, J., Wrasse, C. M., Gobbi, D., Takahashi, H., & Souza, P. (2009). Observation of mesospheric gravity waves at comandante ferraz antarctica station (62 s). In *Annales geophysicae* (Vol. 27, pp. 2593–2598). https://doi.org/10.5194/angeo-27-2593-2009

Bedka, K., Brunner, J., Dworak, R., Feltz, W., Otkin, J., & Greenwald, T. (2010). Objective satellite-based detection of overshooting tops using infrared window channel brightness temperature gradients. *Journal of applied meteorology and climatology*, *49*, 181–202. https://doi.org/10.1175/2009JAMC2286.1

Bluestein, H. B. (1993). *Synoptic-dynamic meteorology in midlatitudes: Observations and theory of weather systems* (p. 594). Taylor & Francis.

Bluestein, H. B., Lindsey, D. T., Bikos, D., Reif, D. W., & Wienhoff, Z. B. (2019). The relationship between overshooting tops in a tornadic supercell and its radar-observed evolution. *Monthly Weather Review*, *147*, 4151–4176. https://doi.org/10.1175/MWR-D-19-0159.1

Browning, K. A., Blyth, A. M., Clark, P. A., Corsmeier, U., Morcrette, C. J., Agnew, J. L., & et al. (2007). The convective storm initiation project. *Bulletin of the American Meteorological Society*, *88*, 1939–1956. https://doi.org/10.1175/BAMS-88-12-1939

Carey, L. D., Schultz, E. V., Schultz, C. J., Deierling, W., Petersen, W. A., Bain, A. L., & Pickering, K. E. (2019). An evaluation of relationships between radar-inferred kinematic and microphysical parameters and lightning flash rates in alabama storms. *Atmosphere*, *10*(12), 796. https://doi.org/10.3390/atmos10120796

Chou, M. Y., Lin, C. C., Yue, J., Tsai, H. F., Sun, Y. Y., Liu, J. Y., & Chen, C. H. (2017). Concentric traveling ionosphere disturbances triggered by super typhoon Meranti (2016). *Geophysical Research Letters*, *44*, 1219–1226. https://doi.org/10.1002/2016GL072205

Cooney, J. W., Bowman, K. P., Homeyer, C. R., & Fenske, T. M. (2018). Ten year analysis of tropopause-overshooting convection using gridrad data. *Journal of Geophysical Research: Atmospheres*, *123*, 329–343. https://doi.org/10.1002/2017JD0277110.1002/2017jd027718

Deierling, W., & Petersen, W. A. (2008). Total lightning activity as an indicator of updraft characteristics. *Journal of Geophysical Research: Atmospheres*, *113*. https://doi.org/10.1029/2007JD009598

de Medeiros, A. F. (2001). *Observaões de ondas de gravidade através do imageamento da aeroluminescência*. Instituto Nacional de Pesquisas Espaciais–INPE-10502-TDI/933.

Drob, D. P., Emmert, J. T., Meriwether, J. W., Makela, J. J., Doornbos, E., Conde, M., & et al. (2015). An update to the horizontal wind model (HWM): The quiet time thermosphere. *Earth and Space Science*, *2*, 301–319. https://doi.org/10.1002/2014EA000089

Emersic, C., Heinselman, P., MacGorman, D., & Bruning, E. (2011). Lightning activity in a hail-producing storm observed with phased-array radar. *Monthly Weather Review*, *139*, 1809–1825. https://doi.org/10.1175/2010MWR3574.1

Fritts, D. C., & Alexander, M. J. (2003). Gravity wave dynamics and effects in the middle atmosphere. *Reviews of Geophysics*, *41*(1). https://doi.org/10.1029/2001RG000106

Garcia, F., Taylor, M. J., & Kelley, M. (1997). Two-dimensional spectral analysis of mesospheric airglow image data. *Applied Optics*, *36*, 7374–7385. https://doi.org/10.1364/AO.36.007374

Gelaro, R., McCarty, W., Suárez, M. J., Todling, R., Molod, A., Takacs, L., & et al. (2017). The modern-era retrospective analysis for research and applications, version 2 (merra-2). *Journal of Climate*, *30*, 5419–5454. https://doi.org/10.1175/JCLI-D-16-0758.1

Giongo, G. A., Bageston, J. V., Figueiredo, C. A. O. B., Wrasse, C. M., Kam, H., Kim, Y. H., & Schuch, N. J. (2020). Gravity wave investigations over comandante ferraz antarctic station in 2017: General characteristics, wind filtering and case study. *Atmosphere*, *11*, 880. https://doi.org/10.3390/atmos11080880

Gong, J., Yue, J., & Wu, D. L. (2015). Global survey of concentric gravity waves in airs images and ecmwf analysis. *Journal of Geophysical Research: Atmospheres*, *120*(6), 2210–2228. https://doi.org/10.1002/2014JD022527

Griffin, S. M., Bedka, K. M., & Velden, C. S. (2016). A method for calculating the height of overshooting convective cloud tops using satellite-based IR imager and Cloudsat cloud profiling radar observations. *Journal of Applied Meteorology and Climatology*, *55*, 479–491. https://doi.org/10.1175/JAMC-D-15-0170.1

Holton, J. R. (1992). An introduction to dynamic meteorology. International geophysical series (3d ed., 48, p. 525). Academic Press

Holton, J. R., & Alexander, M. J. (1999). Gravity waves in the mesosphere generated by tropospheric convention. *Tellus B: Chemical and Physical Meteorology*, *51*, 45–58. https://doi.org/10.1034/j.1600-0889.1999.00005.x

Holton, J. R., & Hakim, G. J. (2012). *An introduction to dynamic meteorology* (88, p. 525). Academic press. https://doi.org/10.1016/C2009-0-63394-8

Jurković, P. M., Mahović, N. S., & Počakal, D. (2015). Lightning, overshooting top and hail characteristics for strong convective storms in central europe. *Atmospheric Research*, *161*, 153–168. https://doi.org/10.1016/j.atmosres.2015.03.020

Kim, Y.-J., Eckermann, S. D., & Chun, H.-Y. (2003). An overview of the past, present and future of gravity-wave drag parametrization for numerical climate and weather prediction models. *Atmosphere-Ocean*, *41*(1), 65–98. https://doi.org/10.3137/ao.410105

Kogure, M., Yue, J., Nakamura, T., Hoffmann, L., Vadas, S. L., Tomikawa, Y., & Janches, D. (2020). First direct observational evidence for secondary gravity waves generated by mountain waves over the Andes. *Geophysical Research Letters*, *47*. e2020GL088845. https://doi.org/10.1029/2020GL088845

Lane, T. P. (2015). Gravity waves: Convectively generated gravity waves. *Encyclopedia of atmospheric sciences* (pp.171–179). https://doi.org/10.1016/B978-0-12-382225-3.00489-8

Lane, T. P., Reeder, M. J., & Clark, T. L. (2001). Numerical modeling of gravity wave generation by deep tropical convection. *Journal of the Atmospheric Sciences*, *58*, 1249–1274. https://doi.org/10.1175/1520-0469(2001)058⟨1249:NMOGWG⟩2.0.CO;210.1175/1520-0469(2001)058<1249:nmogwg>2.0.co;2

Lane, T. P., Reeder, M. J., & Guest, F. M. (2003). Convectively generated gravity waves observed from radiosonde data taken during MCTEX. *Quarterly Journal of the Royal Meteorological Society*, *129*(590), 1731–1740. https://doi.org/10.1256/qj.02.196

Lean, H. W., Roberts, N. M., Clark, P. A., & Morcrette, C. (2009). The surprising role of orography in the initiation of an isolated thunderstorm in southern England. *Monthly Weather Review*, *137*, 3026–3046. https://doi.org/10.1175/2009MWR2743.1

Lighthill, M. (1978). *Waves in fluids*. Cambridge University Press. Retrieved from https://books.google.com.br/books?id=oVXTngEACAAJ

Miller, S. D., Straka, W. C., Yue, J., Smith, S. M., Alexander, M. J., Hoffmann, L., & Partain, P. T. (2015). Upper atmospheric gravity wave details revealed in nightglow satellite imagery. *Proceedings of the National Academy of Sciences*, *112*, E6728–E6735. https://doi.org/10.1073/pnas.1508084112

Naccarato, K. P., & Pinto, J. O. (2009). Improvements in the detection efficiency model for the Brazilian lightning detection network (Brasildat). *Atmospheric Research*, *91*, 546–563. https://doi.org/10.1016/j.atmosres.2008.06.019

Naccarato, K. P., & Pinto, J. O. (2012). Lightning detection in southeastern brazil from the new brazilian total lightning network (brasildat). In *2012 international conference on lightning protection (iclp)* (pp. 1–9).

Nyassor, P. K., Buriti, R. A., Paulino, I., Medeiros, A. F., Takahashi, H., Wrasse, C. M., & Gobbi, D. (2018). Determination of gravity wave parameters in the airglow combining photometer and imager data. *Annales geophysicae*, *36*, 705–715. https://doi.org/10.5194/angeo-36-705-2018

Paulino, I. (2012). *Estudo da propagação de ondas de gravidade na termosféra-ionosféra*. Brasil: Instituto Nacional de Pesquisas Espaciais, São José dos Campos.

Paulino, I., Takahashi, H., Vadas, S. L., Wrasse, C. M., Sobral, J., Medeiros, A., & Gobbi, D. (2012). Forward ray-tracing for medium-scale gravity waves observed during the copex campaign. *Journal of Atmospheric and Solar-Terrestrial Physics*, *90*, 117–123. https://doi.org/10.1016/j.jastp.2012.08.006

Pedoe, D. (1995). *Circles: A mathematical view* (p. 102). Cambridge University Press.

Perwitasari, S., Sakanoi, T., Nakamura, T., Ejiri, M., Tsutsumi, M., Tomikawa, Y., & Saito, A. (2016). Three years of concentric gravity wave variability in the mesopause as observed by imap/visi. *Geophysical Research Letters*, *43*, 11–528. https://doi.org/10.1002/2016GL071511

Picone, J., Hedin, A., Drob, D. P., & Aikin, A. (2002). NRLMSISE-00 empirical model of the atmosphere: Statistical comparisons and scientific issues. *Journal of Geophysical Research*, *107*(A12), 1468. https://doi.org/10.1029/2002JA009430

Press, W. H., Teukolsky, S. A., Vetterling, W. T., & Flannery, B. P. (2007). Numerical recipes. In *The art of scientific computing* (3rd ed., p. 1235). Cambridge university press.

Schultz, C. J., Petersen, W. A., & Carey, L. D. (2009). Preliminary development and evaluation of lightning jump algorithms for the real-time detection of severe weather. *Journal of Applied Meteorology and Climatology*, *48*, 2543–2563. https://doi.org/10.1175/2009JAMC2237.1

Sentman, D., Wescott, E., Picard, R., Winick, J., Stenbaek-Nielsen, H., Dewan, E., & Morrill, J. (2003). Simultaneous observations of mesospheric gravity waves and sprites generated by a midwestern thunderstorm. *Journal of Atmospheric and Solar-Terrestrial Physics*, *65*, 537–550. https://doi.org/10.1016/S1364-6826(02)00328-0

Smith, V. H., Mobbs, S. D., Burton, R. R., Hobby, M., Aoshima, F., Wulfmeyer, V., & Di Girolamo, P. (2015). The role of orography in the regeneration of convection: A case study from the convective and orographically-induced precipitation study. *Meteorologische Zeitschrift*, *24*(1), 83–97. https://doi.org/10.1127/metz/2014/0418

Song, I.-S., Chun, H.-Y., & Lane, T. P. (2003). Generation mechanisms of convectively forced internal gravity waves and their propagation to the stratosphere. *Journal of the Atmospheric Sciences*, *60*(16), 1960–1980. https://doi.org/10.1175/1520-0469(2003)060⟨1960:GMOCFI⟩2.0.CO;210.1175/1520-0469(2003)060<1960:gmocfi>2.0.co;2

Stull, R. B. (1976). Internal gravity waves generated by penetrative convection. *Journal of the Atmospheric Sciences*, *33*, 1279–1286. https://doi.org/10.1175/1520-0469(1976)033⟨1279:IGWGBP⟩2.0.CO;210.1175/1520-0469(1976)033<1279:igwgbp>2.0.co;2

Suzuki, S., Shiokawa, K., Otsuka, Y., Ogawa, T., Nakamura, K., & Nakamura, T. (2007). A concentric gravity wave structure in the mesospheric airglow images. *Journal of Geophysical ResearchAtmosphere*, *112*. https://doi.org/10.1029/2005JD006558

Suzuki, S., Vadas, S. L., Shiokawa, K., Otsuka, Y., Kawamura, S., & Murayama, Y. (2013). Typhoon-induced concentric airglow structures in the mesopause region. *Geophysical Research Letters*, *40*, 5983–5987. https://doi.org/10.1002/2013GL058087

Taylor, M. J., & Hapgood, M. (1988). Identification of a thunderstorm as a source of short period gravity waves in the upper atmospheric nightglow emissions. *Planetary and Space Science*, *36*, 975–985. https://doi.org/10.1016/0032-0633(88)90035-9

Taylor, M. J., & Hapgood, M. (1990). On the origin of ripple-type wave structure in the oh nightglow emission. *Planetary and Space Science*, *38*, 1421–1430. https://doi.org/10.1016/0032-0633(90)90117-9

Taylor, M. J., Ryan, E., Tuan, T., & Edwards, R. (1993). Evidence of preferential directions for gravity wave propagation due to wind filtering in the middle atmosphere. *Journal of Geophysical Research*, *98*, 6047–6057. https://doi.org/10.1029/92JA02604

Torrence, C., & Compo, G. P. (1998). A practical guide to wavelet analysis. *Bulletin of the American Meteorological Society*, *79*, 61–78. https://doi.org/10.1175/1520-0477(1998)079⟨0061:APGTWA⟩2.0.CO;210.1175/1520-0477(1998)079<0061:apgtwa>2.0.co;2

Tsugawa, T., Saito, A., Otsuka, Y., Nishioka, M., Maruyama, T., Kato, H., & Murata, K. (2011). Ionospheric disturbances detected by GPS total electron content observation after the 2011 off the pacific coast of Tohoku earthquake. *Earth Planets and Space*, *63*, 875–879. https://doi.org/10.5047/eps.2011.06.035

Vadas, S. L. (2007). Horizontal and vertical propagation and dissipation of gravity waves in the thermosphere from lower atmospheric and thermospheric sources. *Journal of Geophysical Research*, *112*. https://doi.org/10.1029/2006JA011845

Vadas, S. L., & Azeem, I. (2020). Concentric secondary gravity waves in the thermosphere and ionosphere over the continental united states on 25-26 March 2015 from deep convection. *Journal of Geophysical Research*, *126*, e2020JA028275. https://doi.org/10.1029/2020JA028275

Vadas, S. L., & Fritts, D. C. (2005). Thermospheric responses to gravity waves: Influences of increasing viscosity and thermal diffusivity. *Journal of Geophysical Research: Atmosphere*, *110*. https://doi.org/10.1029/2004JD005574

Vadas, S. L., & Fritts, D. C. (2009). Reconstruction of the gravity wave field from convective plumes via ray tracing. In *Annales geophysicae: Atmospheres, hydrospheres and space sciences* (Vol. 27, p. 147). https://doi.org/10.5194/angeo-27-147-2009

Vadas, S. L., & Liu, H.-l. (2009). Generation of large-scale gravity waves and neutral winds in the thermosphere from the dissipation of convectively generated gravity waves. *Journal of Geophysical Research*, *114*. https://doi.org/10.1029/2009JA014108

Vadas, S. L., Liu, H.-l., & Lieberman, R. (2014). Numerical modeling of the global changes to the thermosphere and ionosphere from the dissipation of gravity waves from deep convection. *Journal of Geophysical Research: Space Physics*, *119*, 7762–7793. https://doi.org/10.1002/2014JA020280

Vadas, S. L., Taylor, M. J., Pautet, P.-D., Stamus, P., Fritts, D. C., Liu, H.-L., & Rampinelli, V. (2009a). Convection: the likely source of the medium-scale gravity waves observed in the oh airglow layer near Brasilia, Brazil, during the spreadfex campaign. *Annales Geophysicae*, *27*, 231. https://doi.org/10.5194/angeo-27-231-2009

Vadas, S. L., Yue, J., & Nakamura, T. (2012). Mesospheric concentric gravity waves generated by multiple convective storms over the north american great plain. *Journal of Geophysical Research: Atmospheres*, *117*. https://doi.org/10.1029/2011JD017025

Vadas, S. L., Yue, J., She, C.-Y., Stamus, P. A., & Liu, A. Z. (2009b). A model study of the effects of winds on concentric rings of gravity waves from a convective plume near fort collins on 11 May 2004. *Journal of Geophysical Research: Atmospheres*, *114*. https://doi.org/10.1029/2008JD010753

Vargas, F., Swenson, G., Liu, A., & Pautet, D. (2016). Evidence of the excitation of a ring-like gravity wave in the mesosphere over the Andes Lidar observatory. *Journal of Geophysical Research: Atmosphere*, *121*, 8896–8912. https://doi.org/10.1002/2016JD024799

Wang, D., Takagi, N., Gamerota, W., Uman, M., & Jordan, D. (2015). Lightning attachment processes of three natural lightning discharges. *Journal of Geophysical Research: Atmospheres*, *120*, 10–637. https://doi.org/10.1002/2015JD023734

Williams, E., Boldi, B., Matlin, A., Weber, M., Hodanish, S., Sharp, D., & Buechler, D. (1999). The behavior of total lightning activity in severe florida thunderstorms. *Atmospheric Research*, *51*, 245–265. https://doi.org/10.1016/S0169-8095(99)00011-3

Wrasse, C. M., Nakamura, T., Takahashi, H., Medeiros, A., Taylor, M. J., Gobbi, D., & et al. (2006). Mesospheric gravity waves observed near equatorial and low? middle latitude stations: Wave characteristics and reverse ray tracing results. *Annales Geophysicae*, *24*, 3229–3240. https://doi.org/10.5194/angeo-24-3229-2006

Wrasse, C. M., Nakamura, T., Tsuda, T., Takahashi, H., Gobbi, D., Medeiros, A., & Taylor, M. J. (2003). Atmospheric wind effects on the gravity wave propagation observed at 22.7°S-Brazil. *Advances in Space Research*, *32*(5), 819–824. https://doi.org/10.1016/S0273-1177(03)00413-7

Wrasse, C. M., Takahashi, H., Medeiros, A. F. d., Lima, L. M., Taylor, M. J., Gobbi, D., & Fechine, J. (2007). Determinaçao dos parâmetros de ondas de gravidade através da análise espectral de imagens de aeroluminescência. *Revista Brasileira de Geofísica*, *25*, 257–265. https://doi.org/10.1590/S0102-261X2007000300003

Xu, J., Li, Q., Yue, J., Hoffmann, L., Straka, W. C., & Wang, C., & et al. (2015). Concentric gravity waves over northern china observed by an airglow imager network and satellites. *Journal of Geophysical Research: Atmosphere*, *120*. https://doi.org/10.1002/2015JD023786

Xu, S., Yue, J., Xue, X., Vadas, S. L., Miller, S. D., Azeem, I., Zhang, S. (2019). Dynamical coupling between hurricane Matthew and the middle to upper atmosphere via gravity waves. *Journal of Geophysical Research: Space Physics*, *124*, 3589–3608. https://doi.org/10.1029/2018JA026453

Yue, J., Hoffmann, L., & Joan Alexander, M. J. (2013). Simultaneous observations of convective gravity waves from a ground-based airglow imager and the airs satellite experiment. *Journal of Geophysical ResearchAtmosphere*, *118*, 3178–3191. https://doi.org/10.1002/jgrd.50341

Yue, J., Miller, S. D., Hoffmann, L., & Straka, W. C. (2014). Stratospheric and mesospheric concentric gravity waves over tropical cyclone Mahasen: Joint AIRS and VIIRS satellite observations. *Journal of Atmospheric and Solar-Terrestrial Physics*, *119*, 83–90. https://doi.org/10.1016/j.jastp.2014.07.003

Yue, J., Perwitasari, S., Xu, S., Hozumi, Y., Nakamura, T., Sakanoi, T., & Rong, P. (2019). Preliminary dual-satellite observations of atmospheric gravity waves in airglow. *Atmosphere*, *10*, 650. https://doi.org/10.3390/atmos10110650

Yue, J., Vadas, S. L., She, C.-Y., Nakamura, T., Reising, S. C., Liu, H.-L., & Li, T. (2009). Concentric gravity waves in the mesosphere generated by deep convective plumes in the lower atmosphere near fort collins, colorado. *Journal of Geophysical ResearchAtmosphere*, *114*. https://doi.org/10.1029/2008JD011244

Yu, Y., Yan, Z., & Hickey, M. P. (2015). Lower thermospheric response to atmospheric gravity waves induced by the 2011 Tohoku tsunami. *Journal of Geophysical Research: Space Physics*, *120*, 5062–5075. https://doi.org/10.1002/2015JA020986

Zechmeister, M., & Kürster, M. (2009). The generalised lomb-scargle periodogram-a new formalism for the floating-mean and keplerian periodograms. *Astronomy & Astrophysics*, *496*, 577–584. https://doi.org/10.1051/0004-6361:200811296

Erratum

In the originally published version of this article, there were minor typos in Tables 1 and 2 and equations 1, 3, and 6. The typos have been corrected and this may be considered the version of record.